



TECHNISCHE
UNIVERSITÄT
WIEN
Vienna | Austria

D I P L O M A T H E S I S

Expansion of Models for Heart Rate Variability beyond the Autonomic Nervous System

Submitted at the Institute for
Analysis and Scientific Computing
Vienna University of Technology

supervised by

Ao.Univ.Prof. Dipl.-Ing. Dr.techn. Felix Breitenecker
and

Univ. Lektor Dipl.-Ing. Dr. Martin Bachler

by

Jennifer Maria Yvonne Straub
Gombrichgasse 3/8
A-1100 Vienna

Vienna December 18, 2018

Signature Supervisor

Signature

Statutory Declaration

I hereby declare, that I have written this Master Thesis independently, that I have completely specified the utilized sources and resources and that I have definitely marked all parts of the work - including tables and figures - which belong to other works or to the internet, literally or extracted, by referencing the source as borrowed.

Eidesstattliche Erklärung

Hiermit erkläre ich, dass die vorliegende Arbeit gemäß dem Code of Conduct, insbesondere ohne unzulässige Hilfe Dritter und ohne Benutzung anderer als der angegebenen Hilfsmittel, angefertigt wurde. Die aus anderen Quellen direkt oder indirekt übernommenen Daten und Konzepte sind unter Angabe der Quelle gekennzeichnet. Die Arbeit wurde bisher weder im In- noch im Ausland in gleicher oder in ähnlicher Form in anderen Prüfungsverfahren vorgelegt.

Vienna, Date

Signature

Abstract

According to the World Health Organisation, diseases of the cardiovascular system (CVS) are currently the main cause of death in high-, middle-, and low-income countries. Therefore, their understanding, prediction, and prevention with the help of non-invasive, cost effective, and quick methods is of great interest.

Analysis of the heart rate and its change over time can give valuable insight into the health status of a patient, and is easily derived from electrocardiogram data. Reduced heart rate variability (HRV) is associated to an increased probability of dying after myocardial infarctions and indicates inflammatory processes in the body. It is symptomatic of mental disorders such as depression and even serves as an indicator for the risk of suffering from burn-out.

Different approaches in modeling and simulation of HRV can provide new insight into the nonlinear interplay of cardiovascular regulation. In this work, three models for HRV are implemented and compared. They include the firing rate of the baroreceptors, respiration, activity of the sympathetic and parasympathetic nervous system, stroke volume, cardiac noradrenaline and acetylcholine concentration, as well as a windkessel model including peripheral resistance and arterial compliance.

First, an existing model for HRV based on respiration and baroreflex activity was implemented and analyzed. A second model was created through adaptation of the first model. For this purpose, sympathetic activity, as well as the pressure curve in the aortic arch and the duration of the systole were adapted. Based on a model for the autonomic response to orthostatic stress, a third model, including three different types of baroreceptors and a dependence on the mean arterial pressure, was implemented as well.

All three models were realized in Simulink 2017b, and their validation is performed based on two 5 minute electrocardiogram (ECG) recordings from 30

subjects. The simulation results are compared to subject data based on the standards of HRV measurement by the Task Force of the European Society of Cardiology and the North American Society of Pacing and Electrophysiology. Each of the three modeling approaches showed specific advantages, disadvantages, and possibilities for further improvement. Lastly, the results once more underline the complex and nonlinear modulation of HRV, and provide basis for extension of HRV models, paving the way for the future usage of model prediction in the field of cardiovascular diseases.

Kurzfassung

Laut Erhebungen der Weltgesundheitsorganisation sind Erkrankungen des Herzkreislaufsystems derzeit die Haupttodesursache, sowohl in Ländern mit hohem, mittlerem, als auch niedrigem durchschnittlichen Einkommen. Folglich besteht großes Interesse an der Analyse, Vorhersage und Vorbeugung ebendieser mit Hilfe von günstigen, nicht-invasiven Verfahren.

Die Analyse der Herzrate und ihrer zeitlichen Veränderung kann schnell mittels Elektrokardiogrammdaten durchgeführt werden und erlaubt wertvolle Rückschlüsse auf den derzeitigen Gesundheitsstatus des Patienten. Eine Verringerung der Herzratenvariabilität (HRV) kann ein Indiz erhöhter Sterblichkeit nach einem Myokardinfarkt sein, entzündliche Prozesse kennzeichnen oder psychische Erkrankungen wie Depression und Burn-out prognostizieren.

Die Analyse, Modellbildung und Simulation der Herzratenvariabilität kann folglich dazu genutzt werden, das nichtlineare Zusammenspiel der kardiovaskulären Regulationsmechanismen besser zu verstehen. In dieser Arbeit werden drei Modelle verglichen, welche die Barorezeptoren, die Atmung, die Aktivität des sympathischen und parasympathischen Nervensystems, das Herzschlagvolumen, die Acetylcholin- und Noradrenalin-Konzentration im Erregungsleitungssystem des Herzens, der periphere Gefäßwiderstand, sowie die arterielle Compliance berücksichtigen.

Zuerst wurde ein existierendes HRV-Modell, basierend auf Barorezeptoraktivität und Atemfrequenz, implementiert. Ein zweites Modell ergab sich durch Verbesserungen im Bezug auf die Sympathikusaktivität, die generelle Form der Blutdruckkurve und die Systolendauer. Ein Modell zur Beschreibung der Auswirkung von orthostatischem Stress auf das autonome Nervensystem diente als Grundlage für ein drittes HRV-Modell. Darüber hinaus besitzt dieses, im Gegensatz zur den anderen Modellen, drei verschiedene Typen von Barorezeptoren.

Die Modelle wurden in Simulink 2017b implementiert und über den Vergleich mit fünfminütigen Elektrokardiogrammaufzeichnungen von 30 Patienten mit Bluthochdruck validiert. Die Quantifizierung der Herzratenvariabilität basiert dabei auf den Vorgaben der Task Force of the European Society of Cardiology and the North American Society of Pacing and Electrophysiology.

Jedes der präsentierten Modelle wies dabei sowohl spezifische Vor-, als auch Nachteile auf, sowie Möglichkeiten für weitere Verbesserungen. Dies unterstreicht erneut die komplexen, nichtlinearen Zusammenhänge der Regulierung der Herzratenvariabilität und ebnet den Weg für zukünftige Modellerweiterungen.

Danksagung

Da diese Arbeit ohnehin genug Prosa enthält, würde ich meinen Dank gerne in lyrischer Form ausdrücken und an dieser Stelle all jenen, die mich auf meinem Weg durch das Studium begleitet haben, ein paar Zeilen aus Liedtexten widmen.

Für Prof. Felix Breitenecker

*The future's in the air
I can feel it everywhere
Blowing with the wind of change. - Scorpions*

Für Martin

*I've heard it said
That people come into our lives for a reason
Bringing something we must learn
And we are led
To those who help us most to grow. - Stephen Schwartz*

Für meine Familie

*Host mit mir dei ganzes Leben immer dei Weisheit teilt
Koa Pflaster auf a Wundn klebt, weil's ohne schneller verheilt
Und hob i gwort auf di im Regen, host di immer beeilt
Weil du nie gnummen host nur geben
Als hättst Flyer verteilt. - Paul Pizzera*

Für Matthias

*Today the world was just an address,
a place for me to live in, no better than all right.
But here you are, and what was just a world is a star,
Tonight. - Leonard Bernstein & Stephen Sondheim*

Für Raffaella, Franziska und Simon

*Love is the answer
At least for most of the questions in my heart
Like why are we here? And where do we go?
And how come it's so hard?
It's not always easy and
Sometimes life can be deceiving,
I'll tell you one thing,
It's always better when we're together. - Jack Johnson*

Für Edwin

*My, my, my inspiration is what you are to me
Inspiration look, see.
And so today, my world it smiles. - Led Zeppelin*

Danke.

Contents

Abstract	iii
Kurzfassung	v
Danksagung	vii
List of Abbreviations	xi
1 Introduction	1
1.1 Motivation	1
1.2 Scope of Work	2
1.3 Aim of the Thesis	3
1.4 Methodical Approach	3
1.5 Thesis Outline	4
2 Background	5
2.1 The Cardiovascular System	5
2.1.1 Anatomy and Physiology of the Heart	5
2.1.2 Controlling Mechanisms of the Cardiovascular System	8
2.1.3 Further effectors of the CVS	14
2.2 Modeling and Simulation	16
2.2.1 System Types	17
2.2.2 Model Design	17
2.2.3 Simulation	18
2.3 State of the Art and Related Work	19
3 Methods	23
3.1 Measures of Heart Rate Variability	23
3.1.1 Time Domain Methods	23
3.1.2 Frequency Domain Methods	25

3.2	Poincaré Plots	26
3.3	Runge-Kutta Methods	28
3.4	Integral Pulse Frequency Modulation Model	29
3.5	The Lilliefors Test and the Wilcoxon Signed Rank Test	30
3.6	The Butterworth Filter	31
4	The Models	33
4.1	Model 1: An HRV model including respiration and baroreflex .	33
4.2	Model 2: An Adapted Seidel and Herzel Model	39
4.3	Model 3: An HRV model with different baroreceptor types . .	42
4.3.1	Model equations	42
4.3.2	Model expansion	45
4.4	Simulation	48
5	Results	51
5.1	Poincaré Plots	51
5.2	Statistical HRV Analysis	53
5.3	Blood Pressure	59
6	Discussion	63
6.1	Conclusion	69
7	Appendix	71

List of Abbreviations

ACE	Angiotensin Converting Enzyme
ANS	Autonomic Nervous System
ANP	Atrial Natriuretic Peptide
AV	Atrioventricular
bpm	Beats per Minute
Ca²⁺	Calcium
CVS	Cardiovascular System
ECG	Electrocardiogram
HCN	Hyperpolarization-activated Cyclic Nucleotide-gated
HF	High Frequency
HRV	Heart Rate Variability
IPFM	Integral Pulse Frequency Modulation
K⁺	Potassium
LF	Low Frequency
NN	Normal-to-Normal
n.u.	Normalized Units
RK	Runge-Kutta
RMSSD	Root Mean Square of successive Differences
RSA	Respiratory Sinus Arrhythmia
SDNN	Standard Deviation of Normal-to-Normal-Intervals
SDSD	Standard Deviation of successive Differences
SV	Stroke Volume
VLF	Very Low Frequency

1 Introduction

Heart rate variability (HRV), the change in time intervals between successive heart beats, reflects the activity of the autonomous nervous system, and gives information about the overall condition of the cardiovascular system. The heart rate does not have the tendency to approximate a steady state, but keeps on changing as a result of non-static physiological and psychological regulatory mechanisms, which are never truly at rest, and interact in a non-linear way. Regions in the spinal chord and the medulla, which are responsible for the regulation of the heart beat, are modulated by higher brain centers and afferent neurons from the cardiovascular system. The information is processed, and from there, the autonomic nervous system regulates the heart rate accordingly. Quick changes are induced by the parasympathetic nervous system, which is able to react almost instantaneously, while the sympathetic nervous system can only modulate cardiac activity with a time delay of a few seconds [34].

HRV is a sign of a healthy cardiovascular system and its ability to adapt to environmental changes. On the contrary, a reduced change between adjacent interbeat times can indicate a multitude of health problems. Numerous studies have shown its association with diseases such as coronary arteriosclerosis, inflammatory processes, depression, burn-out, autonomic dysfunction, and many other pathologies. Especially after myocardial infarction, reduced HRV was shown to be an indicator of mortality. It is important to note that HRV generally decreases with age, and depends on the heart rate, since a higher heart rate results in shorter interbeat intervals, and therefore leaves less time for changes [34].

1.1 Motivation

According to an analysis of the health profiles of all states of the European Union conducted in 2017, diseases of the cardiovascular system are the main

cause of death in Austria, as shown in the following figure 1.1 [40]. The same picture is presented in studies of the whole European Union, where approximately 45 percent of all death cases are related to cardiovascular causes. Similarly, the 2013 Global Burden of Disease study from estimates 17.3 million deaths globally, making it the most common cause of death world wide [50].

Heart rate variability is a sign of a healthy cardiovascular system and its ability to adapt to environmental changes. As HRV can be easily derived from electrocardiogram (ECG) data, great interest lies in attaining a deeper understanding of its nonlinear regulatory mechanisms, among other methods by using the help of modeling and simulation. Creating a model which is complex enough to reproduce important characteristics of HRV, but still simple enough to maintain applicability, can lead to a deeper physiological insight [43]. Consequently, the resulting insights open up new possibilities for diagnostics and therapy [1].

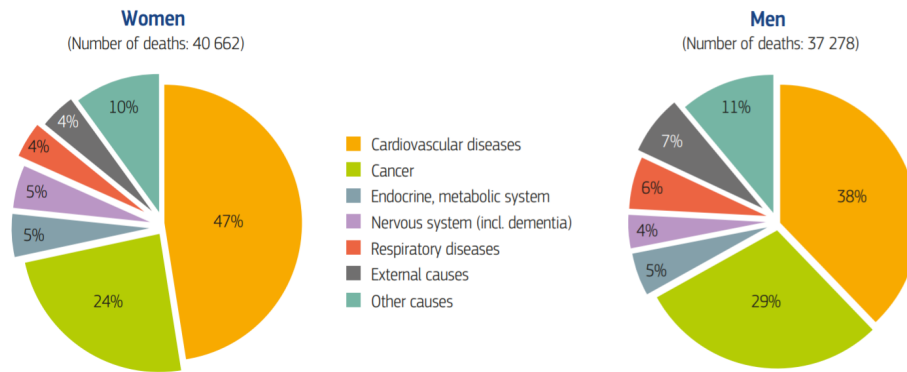


Figure 1.1: Diseases of the cardiovascular system are responsible for the majority of death cases in Austria in 2014. This concerns both male and female population. [40].

1.2 Scope of Work

Existing models for heart rate variability mainly focus on the influence of the autonomic nervous system on the heart [14], neglect vascular components [35], or do not take respiration into account [20], although it has a proven influence on the heart rate [3].

Therefore, the scope of this work is to expand and implement models for heart rate variability, based on existing models. After estimating model parameters

through analysis of given patient data, simulation runs are performed and their outputs are compared to the underlying data based on standard measures for heart rate variability. Via investigation of the models themselves and their simulation results, the following questions shall be addressed:

- Do existing models include physiological processes in a mathematically and medically reasonable way?
- How can the model performance be rated with the help of established measures of HRV?
- Which differences does the simulation output show, compared to data from patients with hypertension, if the most influential model parameters were estimated from the given patient data?
- How can an existing model, which already includes the most common influences on the heart rate, be further expanded and improved, based on this comparison?

1.3 Aim of the Thesis

The goal of this thesis lies in the mathematical expansion, improvement, and application of models of the cardiovascular system, as well as their validation. In the process, the scope mainly lies on creating a realistic representation of heart rate variability. The resulting models are implemented in Simulink 2017b. In order to assess their validity and to estimate possibilities for further improvements, their simulation results are compared to electrocardiographic recordings from patients with hypertension.

1.4 Methodical Approach

In the beginning, a detailed literature research was carried out, as it is not only necessary to get an overview of existing HRV models, but also acquire a well-founded knowledge of the physiological processes behind controlling mechanisms of the heart rate.

A multitude of existing models and submodels of the cardiovascular system was found, with their structure ranging from very fundamental to highly complex. Since numerous parameters need to be estimated in any case, some of the models turned out to be unsuitable for implementation, due to their richness of detail.

Once the models are improved, expanded, and implemented in Simulink

2017b, their performance is assessed via comparison to given data from hypertensive patients. First, model parameters are estimated from the given data, followed by the simulation runs. Their outputs are then analysed based on established measures of heart rate variability.

Interpretation of the obtained results gives valuable insight into strengths and weaknesses of the existing models. This lays the foundation for further improvements and reevaluation.

1.5 Thesis Outline

Chapter 1 specifies the motivation and aim of this thesis. It is followed by a description of the cardiovascular system and the most important regulatory mechanisms of the heart rate in Chapter 2. Chapter 3 deals with the most common measures of heart rate variability, as well as other mathematical principles used later in the thesis. Three models of the cardiovascular system, including expansion and improvement of existing models, are presented in Chapter 4. Validation is performed by comparing the model simulation output to 5 minute heart rate recordings from 30 subjects suffering from hypertension. The results are summarized in Chapter 5, followed by their analysis and interpretation in Chapter 6, which also includes an outlook on possible further improvements. Ultimately, the Appendix contains additional simulation outputs and results.

2 Background

The first section gives a description of the cardiovascular system (CVS) and its physiological controlling mechanisms, followed by a basic definition of the terms modeling and simulation. The chapter is closed by an overview of the current state of the art concerning the modeling and simulation of the CVS.

2.1 The Cardiovascular System

2.1.1 Anatomy and Physiology of the Heart

The human heart consists of two separate pumps: a right heart and a left heart. Each of these two pumps is again divided into two chambers: the atrium, serving as a weak primer pump, and the ventricle, applying the main force to the blood. The right ventricle pumps the blood through the pulmonary circulation, whereas the left ventricle ejects it into the peripheral circulation. Tricuspid and mitral valves prevent backflow from the ventricles into the atria and aortic and pulmonary artery valves prevent backflow from the aorta and pulmonary arteries into the ventricles. The described course of the blood flow through the heart and the cardiovascular system is depicted in figure 2.1. About 80 percent of the blood from the great veins flow directly through the atria into the ventricles, even before the atria contract. Therefore, the ventricular pumping effectiveness is increased by as much as 20 percent by the contraction of the atria. As the heart is capable of pumping 300 to 400 percent more blood than required by the resting body, a malfunction of the atria can stay largely unnoticed, unless a person exercises [25].

One cardiac cycle consists of all the events occurring between two successive heartbeats. It can be divided into four different phases: At the beginning of each cycle, during the contraction phase, the pressure inside the left ventricle rises but is still less than the pressure in the aorta, so the aortic valves stay closed. The second phase is the so called ejection phase, during which

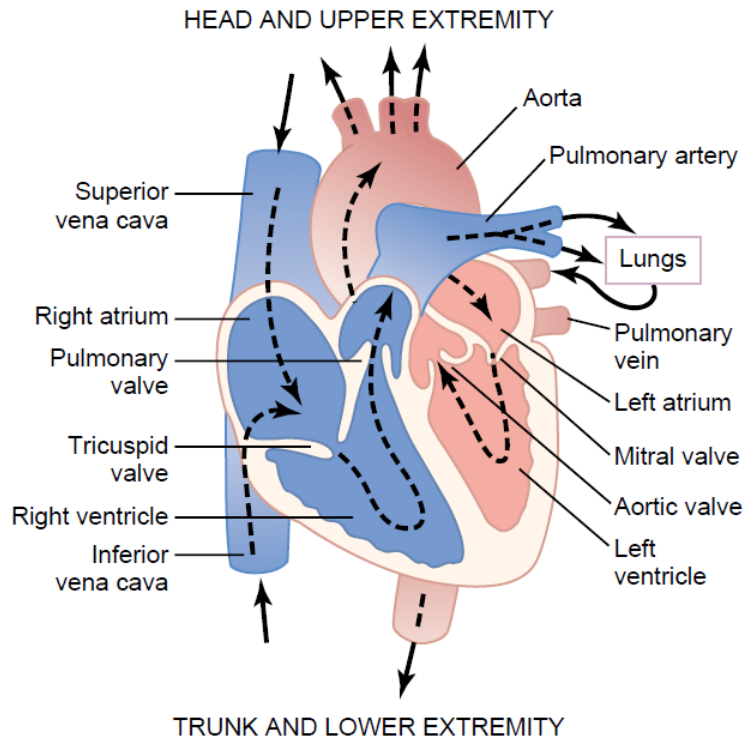


Figure 2.1: Description of the anatomy of the heart and the blood circulation through the heart [25].

around 90ml of blood are pumped out of the ventricle and into the aorta. After the aortic valves close again, the relaxation phase starts. It is followed by the filling phase, which starts after the pressure inside the left ventricle falls below the pressure inside the left atrium. This causes the mitral valves to open and the left ventricle is filled again [41].

More commonly, the heart cycle is divided into a systolic and a diastolic part. The systolic part equals the ejection phase and covers the timespan between the opening and the closing of the aortic valves. On the contrary, the diastole describes the phase of relaxation until the aortic valves open again. It covers the same timespan as relaxation, filling and contraction phase combined [25]. Changes in left atrial and ventricular pressure, as well as aortic pressure, ventricular volume, the electrocardiogram and the phonocardiogram are depicted in figure 2.2. The sinus node is a small, flattened, ellipsoid strip in the posterolateral wall of the right atrium about 3mm wide, 15mm long, and 1mm thick. It is the primary pacemaker of the heart and possesses the capability of self-excitation, causing 60-80 rhythmical contractions per minute. Its fibres contain almost no contractile muscle filaments,

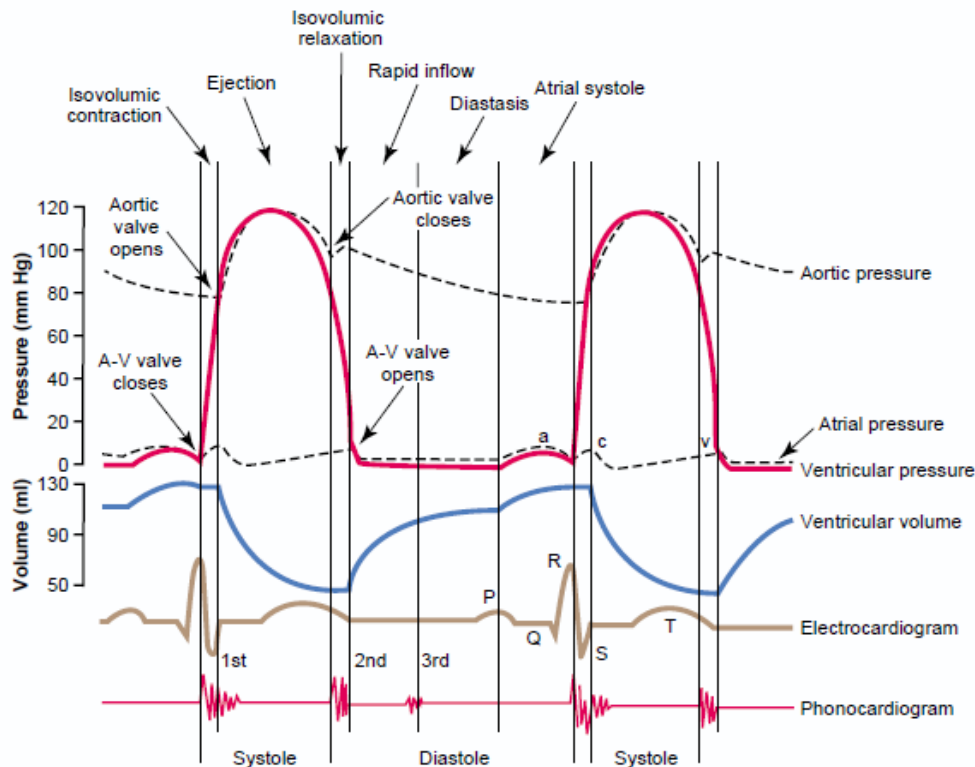


Figure 2.2: Events of the cardiac cycle for left ventricular function [25].

but connect directly with atrial muscle fibers, which leads to an immediate spreading of action potentials. Each impulse passes from the sinus node to the atrioventricular (AV) node, where it is delayed, before passing the AV-bundle and the left and right bundle branches of Purkinje fibers, conducting it further to all parts of the ventricles. The AV node and the Purkinje fibres also possess the capability of self-excitation with a frequency of 40-60 and 20-40 excitations per minute. As a result of this special stimulus conduction, the atria contract first, pushing the blood into the ventricles with a delay of around 0.1 seconds before their contraction begins. This is also referred to as PQ-duration, due to its depiction on the ECG [25].

As mentioned before, cardiac pacemaker cells have the capability of self-excitation because of their unstable resting potential. Opposite to the action potential of skeletal muscle cells, which exists because of stabilising Kalium-channels (K^+ -channels), there is a phase of automatic diastolic depolarisation after each repolarisation. At the end of the repolarisation, when the membrane voltage reaches values below -50mV , the hyperpolarization-activated cyclic nucleotide-gated cation channels (HCN-channels), also called funny

channels, open. These are non-selective ion channels allowing cations, mostly sodium ions (Na^+) to flow into the cell. In combination with the complete absence of potassium channels, which would normally stabilise the resting potential, this causes an automatic depolarisation. Another difference is the absence of fast Na^+ channels. When the threshold of -55mV is reached, a new action potential is created by the influx of calcium ions (Ca^{2+}). This Ca^{2+} influx is slower than the Na^+ influx through fast Na^+ channels. The membrane voltage rises to 30mV , then K^+ -channels open, K^+ -ions flow into the cell and it is repolarized again [41].

The action potential of the heart muscle cells also differs considerably from the action potential of skeletal muscles. Its resting potential lies at -85mV , due to its high potassium (K^+) conductivity. If the voltage rises to the threshold potential of -65mV by excitation from the sinus node, the fast Na^+ channels open, causing a very rapid influx of cations and a rise of the membrane voltage to $+40\text{mV}$. This so called overshoot is followed by a plateau phase, caused by a slow depolarizing Ca^{2+} influx over a duration of 200ms . The Ca^{2+} ions flow into the cell and result in even more Ca^{2+} being released from the intracellular reservoirs. The risen Ca^{2+} concentration inside the cell then leads to its contraction. Therefore, the extra- and intracellular Ca^{2+} concentrations and their changes are the determining factor for the contractility of the heart muscle cell. After that the Ca^{2+} channels close again and K^+ -channels open. The resulting potassium efflux repolarizes the cell and a new action potential can be generated. The whole process takes about 300ms and due to the long refractory period caused by the plateau phase, the maximum heart rate is limited to around 200 beats per minute (bpm) [41].

2.1.2 Controlling Mechanisms of the Cardiovascular System

During rest, the heart beats about 70 times per minute and pumps approximately 4 to 6 liters of blood. When a person is exercising, the heart rate increases up to 180-200 beats per minute and the blood flow is increased up to seven times the normal amount. The heart rate is mainly regulated by the autonomic nervous system and influenced by a multitude of factors such as respiration or stress level. Regulation of the volume pumped by the heart mainly depends on two factors: the intrinsic cardiac regulation depending on the volume of blood flowing into the heart (Frank-Starling-Mechanism) and the control of the heart rate and strength of pumping by the autonomic nervous system [25].

The Frank-Starling-Mechanism

The amount of blood pumped by the heart per minute is largely determined by the rate of blood flow into the heart, the so called venous return. The Frank-Starling mechanism is the intrinsic ability to adapt to increasing volumes of inflowing blood into the heart. A greater stretch of the right heart during filling leads to a stronger contraction, resulting in a greater amount of blood being pumped into the aorta. This is absolutely necessary, because otherwise the right heart would pump more blood into the lungs than the left heart ejects, causing high blood pressure in the pulmonary circulation. In addition to this, the heart rate is further increased by 10 to 20 percent, due to the right atrial walls reaction to stronger stretching, but this mechanism is secondary compared to the Frank-Starling mechanism. Another noteworthy characteristic of this mechanism is its total dependence on the stretch of the heart muscle and therefore independence from neuronal influences [25].

The Autonomic Nervous System

The autonomic nervous system (ANS) consists of two anatomically and functionally distinct divisions: the sympathetic nervous system and the parasympathetic or vagal nervous system. Due to their mostly opposing effect, an increase of sympathetic influence on the heart will simultaneously decrease vagal activity and vice versa, creating a rapid and precise controlling mechanism. The sympathetic system is mainly activated during exercise and emergency situations, preparing the body for physical activity by increasing the heart rate and the blood flow through the system. The parasympathetic system on the other hand is dominant during rest conditions. It regulates basic body functions and decreases the heart rate [33].

The axons of the autonomic nervous system start in the brain stem, run through the spinal cord and are then interconnected to other autonomic neurons in the peripheral autonomic ganglia. Therefore one differentiates between preganglionic and postganglionic neurons.

The sympathetic ganglia are located pairwise along the the spinal cord as a so-called paravertebral chain of gangliae. The preganglionic parasympathetic nerves have their origin in the brain regions of the brain nerves number III (Nervus oculomotoris), VII (Nervus facialis), IX (Nervus glossopharyngeus) and X (Nervus vagus), as well as in the sacral segment of the spinal cord. Their ganglia lie very close or inside of the organ they affect. Both divisions of the ANS release acetylcholine to excite the postganglionic neurons in the ganglia. The vast majority of sympathetic postganglionic neurons then release noradrenaline to excite their effector organs. For vagal postganglionic neu-

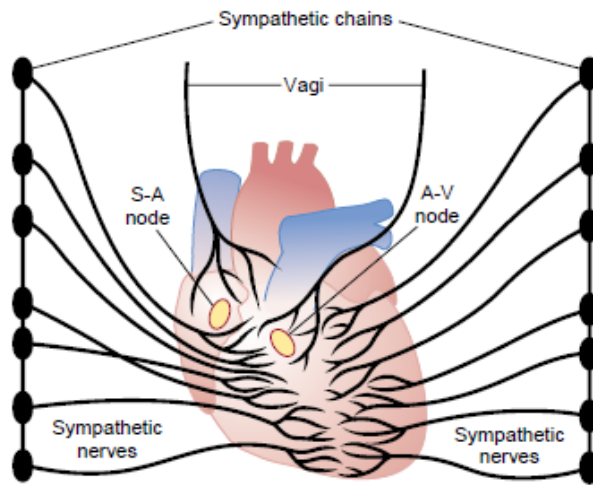


Figure 2.3: Sympathetic and parasympathetic (vagal) nerves of the heart [25].

rons the excitement of their target structures happens through the release of acetylcholine [41].

Efferent nervous activity of the ANS is mostly regulated by autonomic reflexes, for example the baroreceptor reflex, which transmit sensory information to the homeostatic control centers, especially those in the hypothalamus and brainstem. A response is carried out by the transmission of nerve signals, that modify the activity of preganglionic autonomic neurons. Heart rate, blood pressure, and body temperature are only a few of the many variables in the human body, which are monitored and regulated by ANS [33]. The medulla oblongata also plays a central role, as it contains preganglionic sympathetic and parasympathetic neurons and acts as a control center. Both nerve types have a basic activity at all times and show activity fluctuations synchronously to respiration. They are also influenced by afferences from the respiratory neurons of the brain stem, mechanoreceptors, nociceptors and chemoreceptors [25].

The tissues of the heart are innervated by both systems, but opposite to the sympathetic fibres the vagal fibres are mainly distributed to the atria, the sinus node, the AV-node, and not to the ventricles, as shown in figure 2.3 [25]. Through sympathetic stimulation of the heart muscle cells, noradrenaline is released regardless of the stretch of the muscle fibres, which affects the β_1 -receptors of the heart muscles. Through intracellular mechanisms the opening of Ca^{2+} channels becomes more likely, causing stronger contractions. Ca^{2+} is also reabsorbed into the sarcoplasmic reticulum more quickly and

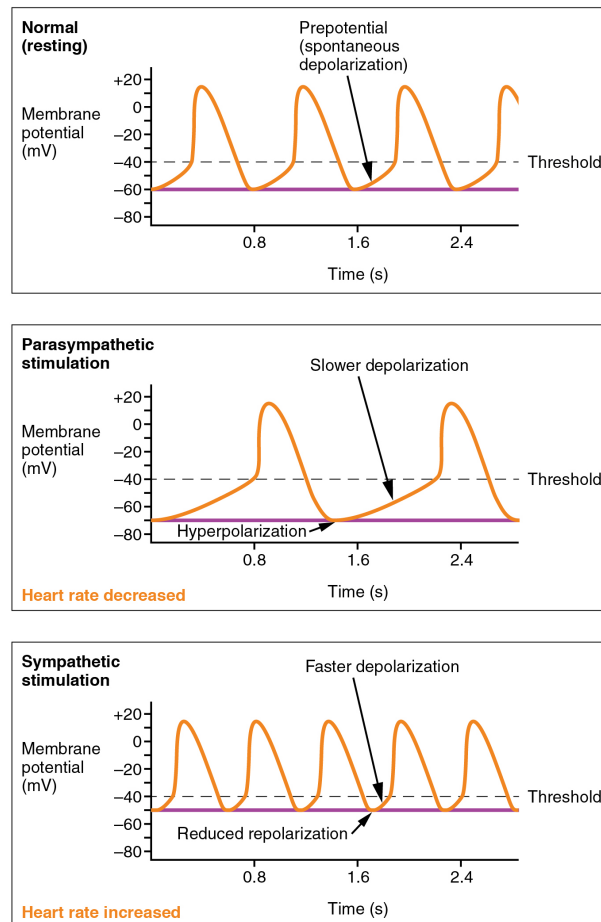


Figure 2.4: Depolarisation of the sinus node depending on the activity of the autonomic nervous system [19].

the muscle fibres are able to relax faster. Parasympathetic activity does not directly influence the contractility of the ventricle myocard, it much rather prevents the release of noradrenaline via presynaptic inhibition and therefore acts as an antagonist. Sympathetic stimulation of the pacemaker cells causes faster depolarisation and therefore a faster HR. The parasympathetic HR reduction comes from a release of acetylcholine at the sinoatrial node and the AV-node, activating the so-called M_2 -receptors, which slow down the diastolic depolarisation through inhibition of the HCN-channels. On the other hand, a higher sympathetic tone causes a release of noradrenaline, which binds to β_1 receptors, accelerates the diastolic depolarisation as well as the excitation of the heart and lowers the threshold for the next depolarisation (see figure 2.4).

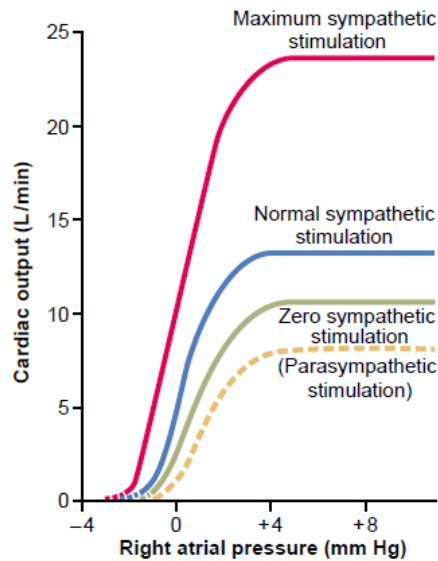


Figure 2.5: Cardiac output and its dependency on right atrial pressure and the ANS activity [25].

The release of sympathetic noradrenaline also affects the blood vessels via α_1 -receptors. After their activation the sarcoplasmic reticulum releases Ca^{2+} ions and therefore the vessel contracts [41].

The cardiac output can be more than doubled by sympathetic stimulation or decreased to as low as almost zero by parasympathetic stimulation, depending on the input atrial pressure as shown in figure 2.5. Under normal conditions, the continuous discharge of sympathetic nerve fibres increases pumping by 30 percent compared to no sympathetic stimulation. The average heart rate for young adults of 70 beats per minute (bpm) can be increased up to approximately 200 bpm by strong sympathetic stimulation, while simultaneously intensifying the contraction to as much as double normal, increasing the amount of blood pumped and augmenting the ejection pressure [25].

Strong parasympathetic stimulation of the heart can even stop the heartbeat, but it normally returns after a few seconds and continues at a rate of 20 to 40 bpm as long as the vagal stimulation lasts. As opposed to the sympathetic stimulation, parasympathetic stimulation decreases the level of cardiac output as much as 30 percent below normal (figure 2.5). As the vagal nerves mainly influence the atria and not the ventricles, the contraction strength is only slightly decreased during parasympathetic stimulation, but even a small change in intensity combined with reduced heart rate can lead to a decrease in ventricular pumping of 50 percent or more [25].

The Baroreflex

The best known subconscious nervous control mechanism for arterial pressure control is the so called baroreceptor reflex. The baroreceptors are spray-type nerve endings located at specific points in the walls of some large systemic arteries, mainly in an area called the sinus caroticus and in the wall of the aortic arch. They generate nervous signals when stretched, i.e. when blood pressure increases, which are then forwarded from the aortic arch to the medulla oblongata of the brain stem through vagal nerves. From there, secondary signals inhibit the vasoconstrictor center of the medula and increase the activity of the vagal parasympathetic center. This leads to a decrease in heart rate, a weaker heart contraction, and vasodilation, that is the enlargement of the diameter of the veins and arterioles of the peripheral circulatory system. This negative feedback reflex mechanism causes a decrease in arterial pressure. Low blood pressure decreases the number of sensory impulses transmitted from the baroreceptors to the vasomotor center, therefore heart rate and vascular resistance increase and blood pressure rises again, causing the oscillation of the baroreceptor reflex [33].

Baroreceptors respond to changes in arterial pressure in a split-second and the intensity of their response can double, for example, if the arterial pressure changes quickly. Variation of arterial pressure is therefore drastically reduced compared to a system without baroreflex. If arterial blood pressure is chronically increased or decreased, the activity of the baroreceptors changes at first, but adapts to the new pressure level in 1 to 2 days. However, their influence on long term blood pressure regulation is still present, since the baroreceptor reflex interacts with the renal-body fluid-pressure control system, causing a gradual decrease in blood volume as a countermeasure against hypertension. If the baroreceptors of the aortic sinus are denervated, the range of variation of the blood pressure extends considerably. After denervating the afferences from the low-pressure system, an additional rise in mean blood pressure can be detected [41]. Aside from respiratory waves, a slower cyclic rise and fall in blood pressure with a duration of 7 to 10 seconds, the vasomotor waves or Mayer waves, can be seen in unanesthetized humans. These waves are caused mainly by oscillations of the baroreceptor reflex. High pressure excites the baroreceptors, which cause a decrease in sympathetic activity and lower the blood pressure with a delay of a few seconds. The baroreceptors detect the decrease in blood pressure and activate the vasomotor center once again, elevating blood pressure. The response is delayed until a few seconds later and another cycle of rising and falling pressure starts [25].

The Effect of Respiration on the Heart

The so called respiratory sinus arrhythmia (RSA) is the synchronous variation of heart rate and respiration. Approximately 10% of the blood in the vascular system is located in the pulmonary circulation and again 10% of the blood inside the pulmonary circulation is distributed in the pulmonary capillary bed, interacting with the alveoli. The stroke volume of the heart is almost equivalent to the blood volume in the capillary bed, therefore most of the blood in the capillary bed is exchanged during each heartbeat. As a consequence, variation of the heart rate during inspiration and expiration affects the efficiency of the gas exchange [56].

A variety of complexly interacting central and peripheral factors cause RSA, but neural mechanisms are dominant compared to nonneural ones to an extent, which allows total RSA elimination by autonomic denervation, as observed for example during heart transplantation [9].

During inspiration, the activity of the efferent cardiac vagal nerve reaches a minimum, causing the intervals between successive heartbeats to shorten, whereas during expiration vagal activity reaches a maximum, resulting in longer intervals. The change in time between successive heartbeats during inspiration and expiration can therefore be an indicator of RSA.

RSA can easily be influenced by cardiopulmonary function, sleep or wakefulness, age, and many other factors [56].

Each inhalation and exhalation usually causes a wavelike rise and fall of the arterial pressure of 4-6 mmHg, called respiratory waves. These waves are caused by several different effects. During inhalation, the pressure in the thoracic cavity drops below normal, causing the blood vessels in the chest to expand, resulting in a reduced blood flow back to the left side of the heart and therefore a decrease of cardiac output and atrial pressure. Another influencing factor is the excitement of vascular and atrial stretch receptors due to respiration related pressure changes. There are more influencing factors causing respiratory pressure waves, but in summary arterial pressure rises during the early part of expiration and decreases during the rest of the respiratory cycle [25].

2.1.3 Further effectors of the CVS

Renal regulation

Low blood volume and therefore a lowered blood pressure results in a lower activity of the baroreceptors, causing enhanced sympathetic tone. The sympathetic nerves also regulate the activity of the kidney. During phases of low

pressure, they are animated to release the enzyme renine. This enzyme separates angiotensin I from angiotensin, which is then converted into angiotensin II by the angiotensin converting enzyme (ACE) in the lung. Angiotensin II then induces a strong vessel contraction, causing blood pressure to rise again. It stimulates the release of Aldosterone from the adrenal cortex, which then enhances the reabsorption of water and Na^+ in the kidneys and counteracts further loss of extracellular volume. In addition, Angiotensin intensifies the feeling of thirst. This mechanism makes drugs that inhibit the activity of the ACE a powerful remedy against high blood pressure.

If blood pressure is high, the walls of the atria are stretched more intensely, resulting in the release of atrial natriuretic peptide (ANP). It acts as an opponent of aldosterone by reducing its release from the adrenal cortex and enhancing the excretion of water and Na^+ .

Since the variation of blood pressure also affects the activity of the baroreceptors and the level of sympathetic tone, it can be seen as an indirect influence on the heart rate [41].

The arterial windkessel effect

The comparatively high pressure in the arterial system is also caused by the relatively low elasticity of the peripheral arterial system. On the contrary, the wall of the thoracic aorta contains a lot of elastic fibres, giving it great extensibility. Therefore, the blood ejected from the heart during systole causes the aorta to stretch, which reduces the systolic pressure rise and therefore has an effect on the baroreceptors. The aorta then returns to its original shape, pushes the blood further into the arterial system and ensures a rather continuous blood flow [41].

Thyroid hormone

The most common sign of augmented thyroid hormone levels is an augmented heart rate during resting conditions. The heart rate usually varies over the course of 24h, but the variation is even stronger for hyperthyroid patients than for healthy subjects. A close correlation between thyroid hormone levels and the heart rate at night can be detected. Combined with the fact that sympathetic tone is at its lowest at night, this indicates a rather direct influence of thyroid hormone on the sino-atrial node activity. Myocardial relaxation, the venous return, the blood volume inside the left ventricle at the end of the diastole, and the stroke volume (SV) are increased by hyperthyroidism [10].

Neurovisceral integration

Vagal tone was shown to be an indicator of a persons ability of attentional control and emotional regulation. It provides information about the efficiency of CNS-ANS neural feedback and can therefore be seen as a measure of ones ability of self-regulation through use of resources and response selection in goal-driven behaviour.

Goal-driven behaviour is, amongst other things, controlled by the so called central autonomic network, which consists of a multitude of reciprocally interconnected brain structures and mediates its output through the autonomic nervous system. It is influenced by visceral, humoral, and environmental informations, and responds according to their changes. This results in a nonlinear dynamical system that mainly affects the heart via the stellate ganglia and the vagus nerve.

Studies have shown that patients suffering from panic anxiety, ineffective emotional regulation, behavioral inflexibility, depression, and anxiety disorder have a reduced HRV as a consequence of their inhibited vagal tone [49].

Age and gender

Analysis of 24-h heart rate variability has shown, that HRV continually decreases with age and very low levels indicate an increased risk of mortality, especially in individuals over the age of 65 years. Male subjects show a greater HRV than age-matched female subjects, especially until the age of 30, but these differences become insignificant by the age of 50 [51].

2.2 Modeling and Simulation

The following section shall give an overview of the basic definitions and principles of modeling and simulation, according to the lecture notes of the lecture 'Modeling and Simulation' at the TU Wien in 2017 [12], if not cited differently.

Generally, modeling and simulation are important tools for finding solutions to scientific problems. Real systems are translated into abstract, mathematical models, making it possible to conduct experiments independent from reality and create simulation results for a variety of problems.

2.2.1 System Types

A system is defined as an integrated whole, consisting of a set of interacting or independent components. It is demarcated from its environment, but can still interact with it via inputs and outputs. The state of a system is characterized by its constants and variables, which can be further divided into exogenous and endogenous, depending on whether they describe the environment or the system itself.

If the behaviour of a system changes depending on input signals, disturbances, and initial values, it is called dynamic. Otherwise, the system is called static. The change of a dynamical systems behaviour is generally not directly proportional to a change in input and disturbances, but dependent on the systems own dynamics. Also, one can often identify subsystems, which interact with one another or influence themselves via feedback loops.

Aside from dynamic systems, one can further draw a distinction between time-discrete, discrete event, continuous, and hybrid systems. Discrete event, continuous and hybrid ones are continuous concerning time, opposite to time-discrete systems. Discrete states are found in discrete event and time-discrete systems, whereas continuous ones show continuous states. Consequently, hybrid systems are characterised by both, the use of discrete and continuous states.

The description of continuous systems often happens via differential equations, which can usually not be solved analytically. Therefore, they need to be discretised, resulting in a discrete computer model, although the underlying system is continuous.

2.2.2 Model Design

A model can be defined as abstract description of a real system, for the purpose of making predictions of a systems behaviour or analysing its characteristics. The process of model design includes deduction and induction. Via deduction, one creates a model based on known laws, such as the laws of physics, resulting in a structural model. A disadvantage of this technique is its tendency to create complex, computationally intensive models. In that case, simplification is achieved with the help of linearisation or removal of negligible terms. Induction is the modeling approach of making assumptions about the models structure and estimating the corresponding parameters, which leads to a so-called behavioral model. The three main principles of model design can be summarised as:

- **Separability:** The system is regarded as separated from its environment and only a part of possible connections are included into the

model.

- **Observability:** One needs to select an interaction of system and environment, which is exact enough to reach the defined goal, but not unnecessarily extensive.
- **Causality:** One needs to assume a strictly causal relation between input, output, and state, that needs to be defined via mathematical relations and equations.

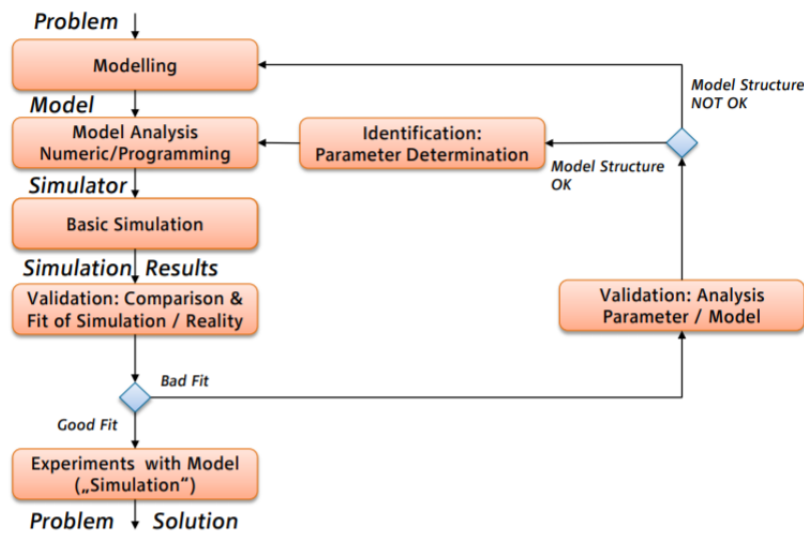


Figure 2.6: The main steps of the cycle of modeling and simulation [12].

2.2.3 Simulation

The definition of simulation, as given by Shannon [45], reads as:

Simulation is the process of designing a model of a real system and conducting experiments with this model for the purpose either of understanding the behavior of the system and its underlying causes or of evaluating various designs of an artificial system or strategies for the operation of the system.

Beside theory and classical experiments, (computer) simulation represents the third pillar of science and is included into the process of problem solving. It is especially relevant if there is not enough theory on the subject, or if one cannot conduct experiments. In the field of medicine, this is often the case

due to ethical reasons, for example if invasive techniques were indispensable for the experiment.

The steps of a simulation study are depicted in figure 2.6. First, the precise formulation of a model for the given problem is of great importance and almost always demands computational implementation, due to its complexity. After conducting the first simulation runs, the model validation is performed. This is the process of comparing first results to the real system to find errors and adapt the model accordingly. Once the model is validated and all parameters are identified, one can perform experiments with it. Finally, the experimental results are used to draw conclusions about the solution of the underlying problem.

2.3 State of the Art and Related Work

A lot of effort has already been put into the modeling and simulation of heart rate variability so far. Existing models include various regulating components of the cardiovascular system and make use of highly statistical approaches [7, 48], as well as differential equations [35], and discrete events [20]. Although all of them try to mimic mechanisms of the human cardiovascular system, a lack of detailed physiological reasoning is found in a lot of them. A common feature of all hereinafter mentioned models lies in the use of an integral pulse frequency modulation (IPFM) model for the generation of a heart beat time series. There is broad consensus about the physiological reasonableness and mathematical applicability of this type of beat generation. IPFM models with constant, as well as varying threshold are found and used in literature [5, 32].

McLernon et al., for example, present a rather simplistic model for generating RR tachograms, including four coupled differential equations of second order, two for the sympathetic and two for the parasympathetic activity of the autonomous nervous system, as input for their IPFM model. Still, they do not give very detailed clarification of the physiological assumptions that led to the respective differential equations and coefficients [35].

Another rather simplistic approach, including the effect of respiration on the heart rate, is presented by Brennan et al. [15]. Aside from two sinusoidal oscillators for the ANS activity, a so-called saw-tooth-oscillator, based on three differential equations, was used as input for the IPFM model of the sinus node. This type of oscillator is characterised by a slow up-stroke and a fast down-stroke, corresponding to slow in- and fast exhalation, as observed in humans. Although this approach for respiration is physiologically reasonable, respiratory influences on the heart rate are usually included into the

parasympathetic activity [23].

Aside from respiration, the baroreflex is often part of heart rate variability models. Olufsen et al. present a model of baroreflex regulation of the heart rate during orthostatic stress, based on not only one, but three types of baroreceptors [39]. Adaptability to different levels of mean blood pressure is given, due to the fact that the baroreceptor differential equations are dependent on previous pressure values. Moreover, this model includes the influence of posture on sympathetic activity via the vestibulo-sympathetic reflex. In contrast to the previous model, respiratory influences on the heart rate are not included in this one.

Instead of including more effectors than the baroreflex, Ursino proposed a compartment model, which includes a more detailed description of the left and right heart, the pulmonary circulation, and their respective resistances and compliances, which are modulated by the activity of the ANS [52].

A more extensive approach is presented by DeBoer, Karemaker, and Strackee [20]. They propose a model based on difference equations, that includes baroreceptor reflex, peripheral resistance, respiration, blood pressure according to a windkessel model, and RR-interval dependent contractility of the myocard. Another particular feature of their model is the absence of an equation for ANS activity. Effectors such as the baroreceptor activity are directly integrated into other equations.

A closed loop model, which includes respiration, the baroreceptor reflex, ANS activity, a windkessel time constant, contractility, and even incorporates the release of neurotransmitters, is proposed by Seidel and Herzel [43]. Opposite to the previously mentioned model, it combines discrete signals, such as the time series of heart beats, and continuous ones, blood pressure for example, and does include equations for sympathetic and parasympathetic activity. Respiration and baroreceptor activity influence both branches of the autonomic nervous system. A unique characteristic of this model is the use of a phase response curve, which modulates the input of the parasympathetic nervous system depending on its time of occurrence during the heart cycle. Models which are highly based on statistics and probability theory often show a lack of interpretability. Barbieri et al. for example suggest an HRV model based on a history-dependent inverse Gaussian process [7]. This may lead to deeper insight about the statistical characteristics of HRV data, but since all regulating effects on the HR are included in the formulation of the history-dependence, little information about the actual physiological processes is used. Similarly, Stanley and Siegel base the input of their IPFM-model on a constant plus a sum of stochastic inputs, such as white noise [47]. Other models include fractal gaussian noise, fractal lognormal noise, fractal binomial noise, and or a source of jitter [48].

A common feature of all mentioned models lies in their focus on modeling macroscopic processes, rather than single cells, although other approaches, especially concerning stimulus conduction in cardiac cells, do exist [18]. This modeling approach probably did not gain popularity, as it leads to computationally intensive simulations.

To conclude, a variety of different modeling approaches exists, and for most parts of the cardiovascular system, no modeling technique was proven to be superior to others yet.

3 Methods

In this chapter, time domain as well as frequency domain methods for quantifying heart rate variability are presented, as well as a mathematical method for solving a first-order ordinary differential equations. A general description of the Integral pulse frequency modulation (IPFM) model is given, followed by the Lilliefors and the Wilcoxon signed rank test, two statistical methods for hypothesis testing.

3.1 Measures of Heart Rate Variability

The description of the following measures is based on the Guidelines of the Task Force of The European Society of Cardiology and The North American Society of Pacing and Electrophysiology [24], if not cited differently.

3.1.1 Time Domain Methods

Time domain methods are statistical techniques for quantification of the change in heart rate, based on the analysis of RR-intervals.

SDNN

An RR-interval is defined as the time between two successive R-peaks of an ECG recording, as shown in figure 3.1. A normal-to-normal interval (NN-interval) is an RR-interval, which does not show any signs of abnormality. The most basic measurement of HRV is the standard deviation of NN-intervals (SDNN), which is equivalent to the square root of variance, and therefore to total spectral power. It includes the low-, as well as the high-frequency components, and is dependent on the duration of the ECG-recording. If a 24h time-interval is analysed, high frequency as well as ultra-low-frequency components are represented by the SDNN, as opposed to 5min recordings, where only shorter cycle lengths can be estimated. Moreover, the total variance of HRV increases with the length of the analysed recording,

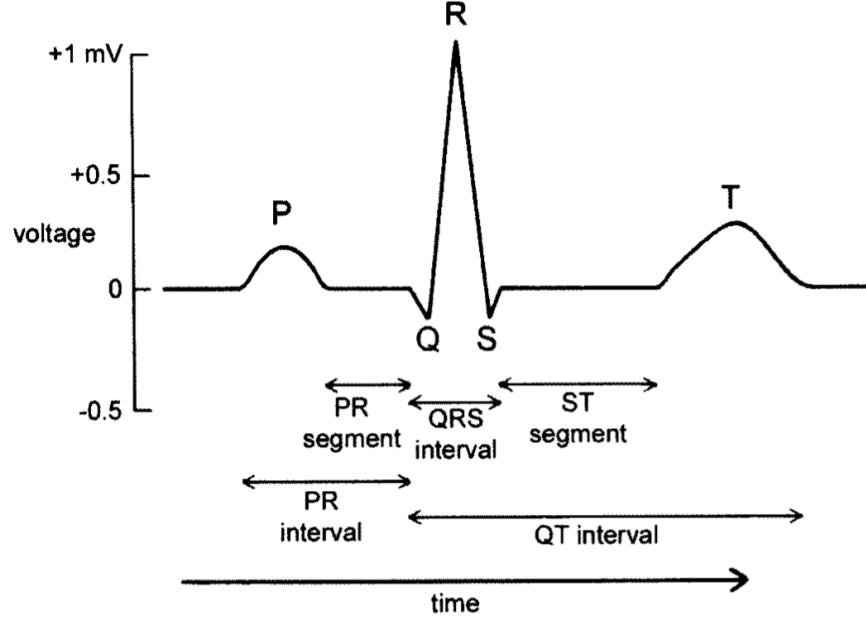


Figure 3.1: A schematic representation of an ECG recording over one cardiac cycle. First the atria depolarize and contract, resulting in the so-called P-wave. The action potential then spreads through the AV-node, causing the ventricles to contract, which generates the QRS-complex. Finally, the T-wave denotes the repolarization of the ventricles, before a new cardiac cycle starts [22].

which is why only SDNN values derived from recordings of the same length can be compared. It is calculated as

$$SDNN = \sqrt{E[NN_n^2] - \overline{NN}^2}. \quad (3.1)$$

RMSSD and SDDSD

Two commonly used HRV-measures are the square root of the mean of the squares of differences between adjacent NN-intervals, and the standard deviation of differences between adjacent NN-intervals (SDSD), which are defined as follows:

$$SDSD = \sqrt{E[\Delta NN_n^2] - \overline{\Delta NN}^2}. \quad (3.2)$$

Assuming that $\overline{\Delta NN} = E[NN_n] - E[NN_{n+1}] = 0$, the equation for the

RMSSD has the following form:

$$RMSSD = \sqrt{E[(NN_n - NN_{n+1})^2]}. \quad (3.3)$$

Both RMSSD and SDDSD reflect high frequency components and correlate to other measures such as $NN50$, the number of interval differences of successive NN-intervals longer than 50ms.

3.1.2 Frequency Domain Methods

For the analysis of short-term HRV recordings, the spectrum is divided into three sections: very low frequency (VLF) below 0.04 Hz, low frequency (LF) from 0.04 Hz to 0.15 Hz and high frequency (HF) components from 0.15 Hz to 0.4 Hz. The power distribution and the central frequency of the LF and HF components change due to autonomic modulation of the heart rate and is usually measured in absolute values of power (ms^2). Describing sympathetic and parasympathetic activity via so-called normalized units (n.u.) is especially useful to emphasize their opposing behaviour, since their power is described in relation to the total power minus the VLF components. The conversion to normalized units also reduces the effects of changes in total power. For short 2 to 5min recordings, the VLF components are not related to certain physiological processes, which modulate the heart rate.

Lomb-Scargle Periodogram

The Lomb-Scargle Periodogram is designed to find periodic signals in unevenly sampled datasets. For a given set of h_i , $i = 1 \dots N$ values, measured at times t_i , in order to derive the periodogram, the mean value, as well as the variance are calculated first [26]:

$$\bar{h} = \frac{1}{N} \sum_1^N h_i, \quad (3.4)$$

$$\sigma^2 = \frac{1}{N-1} \sum_1^N (h_i - \bar{h})^2. \quad (3.5)$$

For each angular frequency of interest $\omega = 2\pi f > 0$, the time-offset τ is calculated:

$$\tan(t\omega\tau) = \frac{\sum_{i=1}^N \sin(2\omega t_i)}{\sum_{i=1}^N \cos(2\omega t_i)}. \quad (3.6)$$

The final spectral power as a function of ω , which gives the Lomb-Scargle-Periodogram, is defined by the following equation:

$$P_N(\omega) = \frac{1}{2\sigma^2} \left\{ \frac{[\sum_{i=1}^N (h_i - \bar{h}) \cos(\omega(t_i - \tau))]^2}{\sum_{i=1}^N \cos(\omega(t_i - \tau))^2} + \frac{[\sum_{i=1}^N (h_i - \bar{h}) \sin(\omega(t_i - \tau))]^2}{\sum_{i=1}^N \sin(\omega(t_i - \tau))^2} \right\}. \quad (3.7)$$

A constant shift of all the t_i values has now effect on $P_n(\omega)$, because the constant τ compensates the shift along the time-axis [26].

3.2 Poincaré Plots

Poincaré plots allow the geometrical analysis, and quantification of HRV by plotting each RR-interval against the following one, resulting in a scatterplot as shown in figure 3.2. Visual analysis of the resulting scatter plot shape can, for example, indicate the degree of heart failure in a patient, and give a quick overview of a large set of RR-interval data [13]. Moreover, ectopic beats and artefacts can be detected easily. This type of plot simultaneously gives an overview of the overall beat-to-beat variability, i.e., the scatter in direction of the x_2 -axis, as well as long-term HRV, which is illustrated by the plots length in x_1 -direction (compare equation 3.8 and figure 3.2) [27]. To characterize the shape of a Poincaré plot, the ellipse fitting technique, often combined with RR-interval histograms, is used. Still, none of these measures is complex enough to reflect the nonlinear dynamics of HRV in detail [13].

SD1 and SD2

In order to characterize the Poincaré plot shape by fitting an ellipse to it, a new set of axis is introduced by rotating the standard axis by $\theta = 45^\circ$

counterclockwise. $SD1$ and $SD2$ are the standard deviations according to the new coordinate system. $SD1$ is interpreted as a measure for short-term HRV, as it quantifies the width of the scatter plot, and is mathematically equivalent to $SDSD$ with a scaling factor. Analogous to this, $SD2$ reflects the long-term HRV, and can be derived from $SDRR$, the standard deviation of RR-intervals, and $SDSD$:

$$\begin{bmatrix} x_1 \\ x_2 \end{bmatrix} = \begin{bmatrix} \cos(\theta) & -\sin(\theta) \\ \sin(\theta) & \cos(\theta) \end{bmatrix} \begin{bmatrix} RR_n \\ RR_{n+1} \end{bmatrix} = \begin{bmatrix} \frac{1}{\sqrt{2}} & -\frac{1}{\sqrt{2}} \\ \frac{1}{\sqrt{2}} & \frac{1}{\sqrt{2}} \end{bmatrix} \begin{bmatrix} RR_n \\ RR_{n+1} \end{bmatrix}, \quad (3.8)$$

$$SD1^2 = Var(x_1) = Var\left(\frac{1}{\sqrt{2}}RR_n - \frac{1}{\sqrt{2}}RR_{n+1}\right) = \quad (3.9)$$

$$\frac{1}{2}Var(RR_n - RR_{n+1}) = \frac{1}{2}SDSD^2, \quad (3.10)$$

$$SD2^2 = 2SDNN^2 - \frac{1}{2}SDSD^2. \quad (3.11)$$

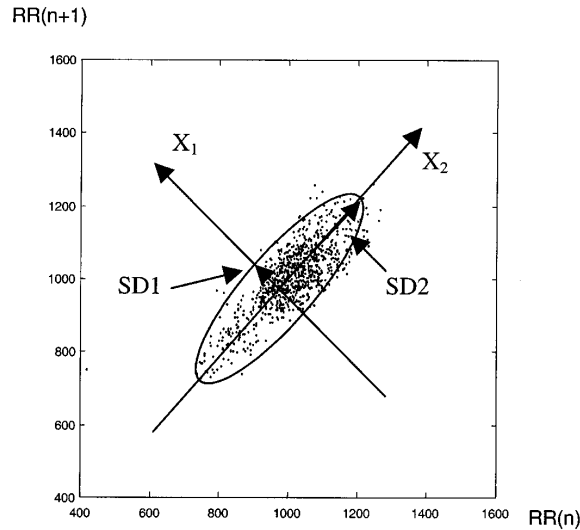


Figure 3.2: An ellipse fitted to an exemplary Poincaré plot. $X1$ and $X2$ denote the new coordinate system, which equals the standard coordinate system rotated by 45 degrees. $SD1$ and $SD2$ represent the standard deviation of the points from the corresponding axes [13].

3.3 Runge-Kutta Methods

The following section is based on the formulations of Dormand and Prince [21], if not cited differently. Assume a system of first-order ordinary differential equations

$$y'(x) = f(x, y(x)) \quad (3.12)$$

with $y(x_0)$ known. Further, $f(x, y(x))$ can be rewritten as $f(y(x))$ without loss of generality. At given points

$$x_{n+1} = x_n + h_n, \quad (3.13)$$

with $n = 0, 1, 2, \dots$, and h_n defined as

$$h_n = \theta(x_n)h \quad 0 < \theta(x_n) \leq 1, \quad (3.14)$$

the approximation \underline{y}_n of the analytical solution $y(x_n)$ can be calculated, if sufficient continuity and differentiability is given. The explicit Runge-Kutta (RK) formula reads as

$$\underline{y}_{n+1} = \underline{y}_n + h_n \Phi(\underline{y}_n, h_n) = \underline{y}_n + \sum_{i=1}^s b_i \underline{k}_i, \quad (3.15)$$

with \underline{k}_1 defined as

$$\underline{k}_1 = h_n f(\underline{y}_n), \quad (3.16)$$

followed by

$$\underline{k}_i = h_n f\left(\underline{y}_n + \sum_{j=1}^{i-1} a_{ij} \underline{k}_j\right) \quad i = 2, 3, \dots, s. \quad (3.17)$$

The integer s denotes the number of stages, a_{ij} is the Runge-Kutta matrix, and b_i are the number of stages of the given method. The approximation of the solution at $x_0 = 0$ corresponds to the given initial value by setting $\underline{y}_0 = y(0)$. The local truncation error \underline{t}_{n+1} at x_{n+1} is given by

$$\underline{t}_{n+1} = \underline{y}(x_n) + h_n \underline{\Phi}(\underline{y}(x_n), h_n) - \underline{y}(x_{n+1}) \quad (3.18)$$

and applying Taylor expansion about x_n to the previous equation, can be rewritten as

$$\underline{t}_{n+1} = h_n (\underline{\Phi}(\underline{y}(x_n), h_n) - \underline{\Delta}(\underline{y}(x_n), h_n)), \quad (3.19)$$

with Δ equaling

$$\underline{\Delta}(\underline{y}(x_n), h_n) = \sum_{r=1}^{\infty} \frac{h^{r-1}}{r!} \underline{y}^r(x). \quad (3.20)$$

A Runge-Kutta formula of p -th order is given, if the local truncation error satisfies

$\underline{t} \leq \mathcal{O}(n^{p+1})$. The equation for \underline{t} can be rewritten as

$$\underline{t}_{n+1} = \sum_{j=1}^{\infty} h_n^{p+j} \underline{\phi}_{p+j-1}(\underline{y}(x_n)). \quad (3.21)$$

With \underline{F}_i^{r+1} denoting the elementary differentials of order $r+1$ of \underline{f} , $\underline{\phi}_r$ equals

$$\underline{\phi}_r(\underline{y}(x)) = \sum_{i=1}^{n_{r+1}} a_i^{r+1} \underline{F}_i^{r+1}(\underline{y}(x)) \quad r = 1, 2, \dots, \quad (3.22)$$

which results in

$$a_i^{r+1} = 0, \quad i = 1, 2, \dots, n_{r+1}, \quad r = 1, 2, \dots, p-1, \quad (3.23)$$

due to the fact that $\underline{\phi}_r = 0$ for $r = 1, 2, \dots, p-1$, if the formula is of order p . For consistency reasons, the following equation has to be satisfied:

$$a_1^1 = \sum_{i=1}^s b_i - 1 = 0, \quad (n_1 = 1). \quad (3.24)$$

These last two equations are general conditions for a Runge-Kutta formula of order p . The Runge-Kutta embedding technique uses two RK formulae of orders p and $q = p + 1$, which share the same function evaluations. The local truncation error in the p th order formula can be calculated, which helps control the step size.

3.4 Integral Pulse Frequency Modulation Model

Many authors assume a modulating effect of the sympathetic and parasympathetic activity on the sino-atrial node, and therefore the heart rate. This influence is summarized as a function $m(t)$ with zero mean and a rather small amplitude, compared to the mean of heart rate. In addition, the modulating function has to be a band-limited signal with negligible power spectral density for frequencies higher than 0.4 Hz. The beat occurrence times t_k generated by the Integral Pulse Frequency Modulation (IPFM) Model can then be written as

$$k = \int_0^{t_k} \frac{1 + m(t)}{T} dt \quad k = 1, 2, 3, \dots, \quad (3.25)$$

or in its continuous analogon

$$x = \int_0^{t(x)} \frac{1 + m(t)}{T} dt, \quad (3.26)$$

with T being the mean RR-duration and t_k denoting the occurrence time of the k -th heartbeat for both formulations. This means, that once the integral reaches a threshold of 1, a new heartbeat is generated and the integrator is reset to zero. Moreover, it is assumed, that the first beat occurs at $t = 0$. Although the threshold is usually set to 1, principally any positive function can be used as threshold [32].

3.5 The Lilliefors Test and the Wilcoxon Signed Rank Test

The Lilliefors test is used to test the null hypothesis, that a one-dimensional probability distribution equals a reference probability distribution. In most cases one wants to verify whether or not a given data sample containing N observations comes from a normal distribution. Therefore, one determines

$$D = \max_X |F^*(X) - S_N(X)|, \quad (3.27)$$

with $S_N(X)$ being the cumulative distribution of the sample and $F^*(X)$ being the cumulative normal distribution function with an estimates mean value $\gamma = \bar{X}$ and a variance equalling that of the sample $\sigma^2 = s^2$. If the value D exceeds a certain critical value, which is based on results obtained from Monte Carlo calculations for different sample sizes, the null hypothesis is rejected and one can no longer assume that the dataset comes from a distribution specified by $F^*(X)$ [28].

The Wilcoxon signed rank test is a two-sided test for the null hypothesis that $X_1 - X_2$ comes from a distribution with zero median. The datasets X_1 and X_2 do not need to come from a normal distribution, as would be necessary for the Students t-test. First, the rank R_i is calculated for the absolute differences $D_i = |x_{i,1} - x_{i,2}|$, followed by the positive and negative rank sums

$$W_+ = \sum_{i=1}^n I(x_{i,1} - x_{i,2} > 0) R_i \quad (3.28)$$

$$W_- = \sum_{i=1}^n I(x_{i,1} - x_{i,2} < 0) R_i \quad (3.29)$$

with I being the indicator function. If $x_{i,1} - x_{i,2} = 0$ for some i , half of the corresponding rank value is added to W_+ and W_- , respectively. W equals the minimum of W_+ and W_- and is then compared to a critical value from a reference table. The null hypothesis is rejected, if $|W| > W_{critical}$ [16].

3.6 The Butterworth Filter

In contrast to other filters, the Butterworth filter was designed by Stephen Butterworth in 1930 for the purpose of signal processing with a maximally flat frequency response in the passband. Its normalized transfer function reads as

$$A[P] = \frac{A_0}{\prod_i (1 + a_i P + b_i P^2)} \quad (3.30)$$

with $P = \frac{p}{\omega_0}$, ω_0 being the cutoff frequency, and A_0 being the DC voltage gain. If n , the order of the filter, is an even number there holds

$$i = 1, \dots, \frac{n}{2}, \quad (3.31)$$

$$a_i = 2 \cos \frac{(2i-1)\pi}{2n}, \quad b_i = 1. \quad (3.32)$$

Analogously, if n is an odd number, the coefficients are defined as

$$i = 2, \dots, \frac{n+1}{2}, \quad a_1 = 1, \quad b_1 = 0, \quad (3.33)$$

$$a_i = 2 \cos \frac{(i-1)\pi}{n}, \quad b_i = 1. \quad (3.34)$$

This leads to a uniform sensitivity with respect to the wanted frequencies. The frequency response rolls off towards zero in the stopband, the faster the higher the filter order is chosen [17].

4 The Models

In the following sections three HRV-models are introduced: First, an HRV-model by Seidel and Herzl [43], which was designed to simulate HRV due to respiration, is presented. Secondly, based on their findings, an adapted version of their model is developed. Thirdly, a model for HRV under orthostatic stress by Olufsen et al. [39] is presented and expanded.

4.1 Model 1: An HRV model including respiration and baroreflex

In this section, the nonlinear HRV model presented by Henrik Seidel and Hanspeter Herzl [43] is described. A schematic depiction of the model subsystems is given in figure 4.1.

Model equations

As the firing rates of fibres of the autonomic nervous system have values around $4\text{-}5\text{s}^{-1}$, it is difficult to model neuronal activity on scales which range from seconds to milliseconds. It is therefore hardly possible to create a model based on firing rates and single spikes, especially with insufficient knowledge of medullary processes. For those elements highly sensitive to the timing of the next spike, the exact moment of its occurrence should be derived from a probability distribution, which is based on the firing frequency. Since nerves usually consist of several nerve fibres, which have the same firing frequency on greater timescales, an overall nerve fibre activity ν can be approximated by letting the number of nerve fibres N approach infinity:

$$\nu = \lim_{\delta t \rightarrow 0} \frac{1}{\delta t} \lim_{N \rightarrow \infty} \frac{N(\delta t)}{N}. \quad (4.1)$$

$N(\delta t)$ denotes the number of nerve fibres firing during the time interval δt . This approximation holds as long as $N \gg \frac{1}{\tau f}$. Assuming that τ is the impulse

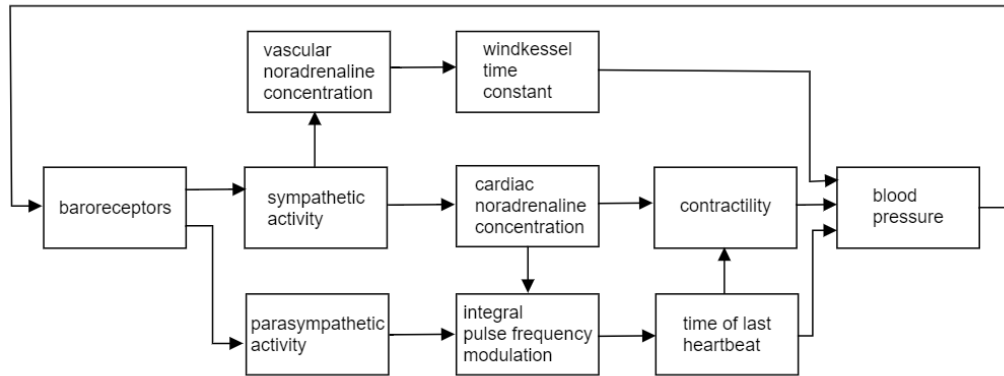


Figure 4.1: Schematic representation of the CVS model in [43].

duration with a value of around 1ms, and that the mean firing rate f lies at $5s^{-1}$, more than 200 nerve fibres per nerve are necessary. This is generally assumed in the model bei Seidel and Herzl.

The baroreceptors

The baroreceptors do not only detect the absolute deviation of the current bloodpressure from the default value p_0 , but also the rate of change. Hence, they are modeled as proportional, as well as differential sensors, and therefore their firing rate can be described as

$$\nu_b = k_1(p - p_0) + k_2 \frac{dp}{dt}, \quad (4.2)$$

with k_1 and k_2 being model parameters (see table 4.1).

Sympathetic and parasympathetic activity

The medullary processes are not modelled in great detail, and in order to keep the model as simple as possible, a linear dependence of the acitivity of the autonomous nervous system on the activity of the baroreceptors is assumed.

In this model, the interaction between respiration and baroreceptor loop is restricted to only one location, and only medullary neuronal influences of respiration are taken into account. Therefore it is negligible during which phase of in- or expiration the autonomic activity is augmented or reduced, as a badly chosen activating phase range of the respiratory cycle only shifts

the in- and expiration, but leaves the dynamics unchanged. The sympathetic activity ν_s and the parasympathetic activity ν_p ,

$$\nu_s = \max(0, \nu_{s,0} - k_{s,b}\nu_b + k_{s,r}|\sin(\pi f_r t + \Delta\phi_{s,r})|), \quad (4.3)$$

$$\nu_p = \max(0, \nu_{p,0} + k_{p,b}\nu_b + k_{p,r}|\sin(\pi f_r t + \Delta\phi_{p,r})|), \quad (4.4)$$

both have a resting-tone $\nu_{s,0}$ and $\nu_{p,0}$, and are influenced by the baroreceptor activity ν_b . As the bloodpressure rises, causing the baroreceptors to be activated, ν_s is reduced, and ν_p is increased. The third term represents the modulation caused by respiration. Since it is assumed that these three factors are linearly integrated by neurons of the circulation centers, the maximum function is applied in order to prevent negative values.

The cardiac noradrenaline concentration

As depicted in figure 2.2, the vagal nerves mainly influence the contraction of the atria as opposed to the sympathetic nerves, which innervate the ventricles. The parasympathetic influence is therefore neglected. Since noradrenaline has slow dynamics, a cardiac noradrenaline concentration c_{cNa} is introduced, as well as a time delay τ_{cNa} . This time lag is necessary, since there is a finite nervous conduction velocity from the medulla to the heart, and noradrenaline itself needs a little time to cause an effect on the contraction of the heart. It is modelled as

$$\frac{dc_{cNa}}{dt} = -\frac{c_{cNa}}{\tau_{cNa}} + k_{c_{cNa},s}\nu_s(t - \theta_{cNa}). \quad (4.5)$$

The contractility

Not only do the cardiac muscles tire at high heart rates, resulting in reduced contractility, but also does the potassium conductivity change, which speeds up the next repolarisation, and therefore also reduces contractility S_i . The duration of the last heart cycle is denoted as T_{i-1} , and \hat{S} describes the saturation point of the function defined by the fraction in equation 4.7. With S_0 , $k_{S,c}$, and $k_{S,t}$ being model parameters according to table 4.1, the contractility equations are defined as follows:

$$S'_i = S_0 + k_{S,c}c_{cNa} + k_{S,t}T_{i-1}, \quad (4.6)$$

$$S_i = S'_i + (\hat{S} - S'_i) \frac{S_i'^{n_s}}{S_i'^{n_s} + \hat{S}^{n_s}}. \quad (4.7)$$

The chronotropic effect

In order to create a model which operates on time scales smaller than one heart cycle, a phase φ of the sinus node is introduced. It is influenced by the sympathetic and parasympathetic activity f_s and f_p . This part of the model follows the concept of an IPFM-model. Each time φ reaches the threshold 1, a new heart beat is generated, and φ is set to zero again. The contractility S_i is then added to the last diastolic bloodpressure before the new heartbeat was created, resulting in the new systolic pressure. With T_0 , k_φ , \hat{c}_{cNa} , n_{cNa} , $k_{\varphi,p}$, $\hat{\nu}_p$, and n_p chosen according to table 4.1, the input for the IPFM reads as follows:

$$f_s = 1 + k_{\varphi,cNa} \left(c_{cNa} + (\hat{c}_{cNa} - c_{cNa}) \left(\frac{c_{cNa}^{n_{cNa}}}{\hat{c}_{cNa}^{n_{cNa}} + c_{cNa}^{n_{cNa}}} \right) \right), \quad (4.8)$$

$$f_p = 1 - k_{\varphi,p} \left(\nu_{p,\theta_p} + (\hat{\nu}_p - \nu_{p,\theta_p}) \left(\frac{\nu_{p,\theta_p}^{n_p}}{\hat{\nu}_p^{n_p} + \nu_{p,\theta_p}^{n_p}} \right) \right) F(\varphi), \quad (4.9)$$

$$\frac{d\varphi}{dt} = \frac{1}{T_0} f_s(t) f_p(t). \quad (4.10)$$

Note that $\nu_{p,\theta_p} \equiv \nu_p(t - \theta_p)$. The phase-effectiveness curve $F(\varphi)$ of the parasympathetic influence was chosen as depicted in figure 4.2. It was presented by Reiner et al. [54] in a mathematical model of the sinus node:

$$F(\varphi) = \varphi^{1.3} (\varphi - 0.45) \frac{(1 - \varphi)^3}{(1 - 0.8)^3 + (1 - \varphi)^3}. \quad (4.11)$$

This curve is necessary to account for the different effects of vagal activity, depending on when during the heart cycle it occurs. Seidel and Herzog note, that $F(\varphi)$ should actually be a function of the whole history of the modeled system, but to keep the model simple it was chosen as a function of one heart phase only.

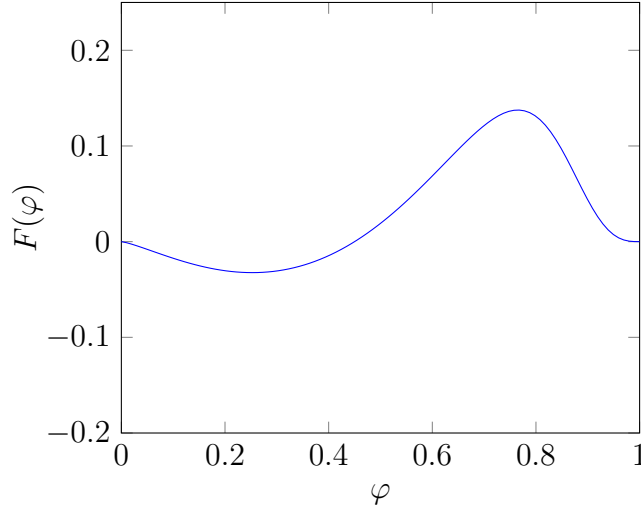


Figure 4.2: The phase effectiveness curve.

Modeling of the Vascular System

High sympathetic activity also affects the blood vessels via an increased release of noradrenaline. As a consequence, the contraction of the vessels intensifies, and the peripheral resistance rises. A differential equation for the vascular noradrenaline concentration c_{vNa} , similar to the one introduced for the cardiac noradrenaline concentration, is formulated:

$$\frac{dc_{vNa}}{dt} = -\frac{c_{vNa}}{\tau_{vNa}} + k_{c_{vNa},s}\nu_s(t - \theta_{vNa}). \quad (4.12)$$

The time delay of the sympathetic activity, denoted as τ_{vNa} , and the parameter $k_{c_{vNa},s}$ are chosen according to table 4.1. The windkessel time constant τ_v is then derived from the vascular noradrenaline concentration via

$$\tau_v = \tau_{v,0} + 1.5 \left(c_{vNa} + (\hat{c}_{vNa} - c_{vNa}) \frac{c_{vNa}^{n_{vNa}}}{\hat{c}_{vNa}^{n_{vNa}} + c_{vNa}^{n_{vNa}}} \right). \quad (4.13)$$

Again, $\tau_{v,0}$, \hat{c}_{vNa} , c_{vNa} are parameters chosen according to table 4.1. During systole of each heart cycle, the blood pressure is described as follows:

$$p_I = d_{i-1} + S_i \left(\frac{t - t_i}{\tau_{sys}} \right) \exp \left(1 - \frac{t - t_i}{\tau_{sys}} \right). \quad (4.14)$$

Hereby, d_{i-1} represents the pressure at the end of the last diastole, t_i equals the point in time at which the current cardiac cycle started, and τ_{sys} denotes the systolic duration (see table 4.1). For the diastolic part of the puls wave,

exponential decay according to the windkessel model is assumed, which is defined by

$$\frac{dp_{II}}{dt} = -\frac{p_{II}}{\tau_v(t)}. \quad (4.15)$$

Standard model parameters

The following table sums up all the parameters used by Seidel and Herzel. They were either determined empirically or based on physiological observations.

Table 4.1: Table of standard parameter set of model by Seidel and Herzel [43].

Parameter	Value	Parameter	Value
p_0	50 mmHg	$k_{c_{vNa},s}$	1.2
k_1	$0.02 \frac{1}{\text{mmHg}}$	θ_{vNa}	1.65 s
k_2	$0.00125 \frac{s}{\text{mmHg}}$	θ_p	0.5 s
$\nu_{s,0}$	0.8	S_0	25 mmHg
$k_{s,b}$	0.7	$k_{S,c}$	40 mmHg
$k_{s,r}$	0.1	$k_{S,t}$	$10 \frac{\text{mmHg}}{s}$
f_r	$0.2 \frac{1}{s}$	n_s	2.5
$\Delta\phi_{s,r}$	0.0	\hat{S}	70.0 mmHg
$\nu_{p,0}$	0.0	T_0	1.1 s
$k_{p,b}$	0.3	$k_{\varphi,cNa}$	1.6
$k_{p,r}$	0.1	\hat{c}_{cNa}	2.0
$\Delta\phi_{p,r}$	0.0	n_{cNa}	2.0
τ_{cNa}	2.0 s	$k_{\varphi,p}$	5.8
$k_{c_{cNa},s}$	1.2	$\hat{\nu}_p$	2.5
θ_{cNa}	1.65 s	n_p	2.0
τ_{vNa}	2.0 s	$\tau_{v,0}$	2.2 s
θ_v	1.5 s	\hat{c}_{vNa}	10.0
n_{vNa}	1.5	τ_{sys}	0.125 s

4.2 Model 2: An Adapted Seidel and Herzel Model

The following paragraphs describe a second model, based on the one presented in the previous section, but with the aim of creating a more physiologically accurate model.

Blood pressure and systolic duration

The blood pressure curve generated by the Seidel and Herzel model shows a very sharp peak at the end of the systole, where the pressure also reaches its maximum followed by an abrupt, steep exponential decay. This does not represent physiological reality, since blood pressure starts to decrease even before the beginning of the diastole due to reduced blood flow from the heart. If anything, a discontinuity in the time derivative of the blood pressure function, as seen at the end of the systole, should not occur at the maximum pressure, but when the aortic valves close due to a lack of output from the left ventricle. Moreover, the systolic duration τ_{sys} was estimated at 125ms, which is clearly too short compared to results from in vivo studies, and was therefore set to 300ms [8]. The presented blood pressure submodel does not accurately represent physiological realities, and the equation for systolic pressure in equations 4.16 was replaced by the following equation, which does not show the previously mentioned insufficiencies:

$$p_I = d_{i-1} + S_i \left(\frac{1.8(t - t_i)}{\tau_{sys}} \right) \exp \left(1 - \frac{1.8(t - t_i)}{\tau_{sys}} \right). \quad (4.16)$$

Sympathetic activity

Equation 4.3 includes the absolute value of a sine function, creating a sharp change in sympathetic activity every $\frac{1}{s_f}$ seconds. In order to further improve the model, the summand was replaced by a standard sinusoidal function with frequency s_f , so that the amplitude still ranges between 0 and 1, but without discontinuities in the first derivative. This leads to the following expression:

$$\nu_s = \max \left(0, \nu_{s,0} - k_{s,b}\nu_b + k_{s,r} \frac{\sin(\pi s_f t + \Delta\phi_{s,r}) + 1}{2} \right). \quad (4.17)$$

Secondly, a similar problem occurs when $k_{s,b}\nu_b$ is subtracted in equation 4.3, since ν_b directly depends on the blood pressure curve, which shows abrupt changes at the end of the diastole. To overcome this insufficiency, a but-terworth low-pass filter is introduced, using order 3 and a passband edge frequency of $0.15 \cdot 2\pi \frac{rad}{sec}$, corresponding to the low frequency domain, which represents sympathetic activity according to the Guidelines of the Task Force of The European Society of Cardiology and The North American Society of Pacing and Electrophysiology [24]. In addition to this, the filter output is multiplied by 0.4, to keep a reasonable level of sympathetic activity.

Parasympathetic activity and respiration

Since parasympathetic activity is closely linked to respiratory sinus arrhythmia, the given breathing pattern is only included into this part of the autonomic nervous system model [3]. Assuming that the breathing pattern is represented by a continuous function $r(t)$, ranging from -1 at total expiration to 1 at total inspiration, a linear dependence of parasympathetic activity on respiration is assumed. The sinusoidal function presented in equation 4.4 is replaced similar to the sympathetic case, but without the addition of 1 in the nominator:

$$\nu_s = \max \left(0, \nu_{p,0} + k_{p,b}\nu_b + k_{p,r} \left(\frac{\sin(\pi p_f t + \Delta\phi_{p,r})}{2} + \frac{r(t)}{2} \right) \right). \quad (4.18)$$

This is due to the fact, that summation of the non-negative function $r(t)$ would otherwise lead to an increased overall level of parasympathetic activity. Moreover, the parasympathetic activity has its own basic frequency p_f .

Correction of the mean heart rate

In order to accurately reproduce the mean heart rate defined by T_0 , the product of f_s and f_p as presented in equation 4.10 should equal 1 in the long term. To ensure this behaviour in a computationally reasonable way, the input of the IPFM model is scaled in the following way:

$$m(t) = \frac{1}{10} \int_{t-10}^t f_s(t) f_p(t) dt, \quad (4.19)$$

$$\frac{d\varphi}{dt} = \frac{1}{T_0} \cdot \frac{f_s(t)f_p(t)}{m(t)}. \quad (4.20)$$

The mean level of ANS activity over the last 10 seconds is computed and used to scale the IPFM input to approximately 1. This way, the ratio of sympathetic and parasympathetic activity is maintained, while still allowing ANS activity fluctuations, and keeping approximately the same mean heart rate as specified by T_0 .

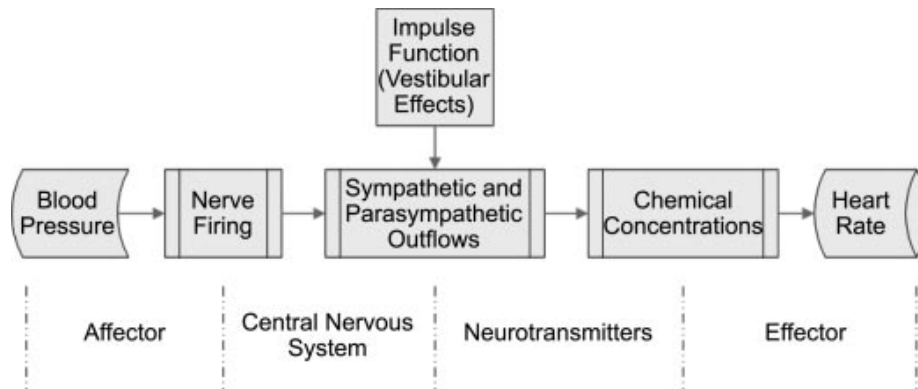


Figure 4.3: Schematic representation of the baroreflex model in [39].

4.3 Model 3: An HRV model with different baroreceptor types

In this section, the model presented by Olufsen et al. [39] is described and extended. It was designed to derive ANS activity and thus heart rate from measured blood pressure values during periods of orthostatic stress. Its basic structure is depicted in figure 4.3.

4.3.1 Model equations

Baroreceptors

Compared to the Seidel and Herzel model, the baroreceptors are modelled in much greater detail by Olufsen et al. They differentiate between three different types of baroreceptors and use translated firing rate curves for elderly people, since hypertension causes a shift of the pressure-response-curve to the right along the pressure axis. The model is not based on the rate of pressure change and its current deviation from a standard value, but on the rate of change of mean arterial pressure, which is denoted as \bar{p} :

$$\bar{p}(t) = \alpha \int_{-\infty}^t p(s) e^{-\alpha(t-s)} ds \quad (4.21)$$

The parameter α hereby describes how strongly the pressure is dependent on previous pressure values, and is set as described in table 4.2. From this definition, one can derive a differential equation for the mean arterial pressure as follows, assuming that the function $p(s)$ is continuous and bounded, by using the integral rule of Leibniz.

$$\frac{d\bar{p}}{dt} = \alpha \left(\frac{d}{dt} \int_{-\infty}^t p(s) e^{-\alpha(t-s)} ds \right) = \quad (4.22)$$

$$\alpha \left(\underbrace{- \int_{-\infty}^t \alpha p(s) e^{-\alpha(t-s)} ds}_{-\bar{p}} + p(t) e^{-\alpha(t-t)} - \underbrace{\lim_{s \rightarrow -\infty} p(s) e^{-\alpha(t-s)}}_{\rightarrow 0} \right) = \quad (4.23)$$

$$= \alpha(p - \bar{p}). \quad (4.24)$$

The change in \bar{p} is directly proportional to the change of n_S , n_I and n_L , which describe the deviation from the average firing rate N . In this case, S stands for short, I for intermediate, and L for long time scales. They represent the variations in threshold for different baroreceptor types and are included into the equations via τ_S , τ_I , and τ_L . The maximum firing rate is taken into account by M , which is set to 120 for all simulations. For the overall firing rate n , there holds $n = n_S + n_I + n_L + N$, with the three baroreceptor differential equations written as follows:

$$\frac{dn_S}{dt} = k_S \frac{d\bar{p}}{dt} \frac{n(M-n)}{(M/2)^2} - \frac{n_S}{\tau_S}, \quad (4.25)$$

$$\frac{dn_I}{dt} = k_I \frac{d\bar{p}}{dt} \frac{n(M-n)}{(M/2)^2} - \frac{n_I}{\tau_I}, \quad (4.26)$$

$$\frac{dn_L}{dt} = k_L \frac{d\bar{p}}{dt} \frac{n(M-n)}{(M/2)^2} - \frac{n_L}{\tau_L}. \quad (4.27)$$

The parameters k_S , k_I , k_L , τ_S , τ_I , τ_L were set according to table 4.2.

The autonomous nervous system

This empirical submodel describes the afferent effect of the baroreceptors on the ANS, based on well known experimental facts. The parasympathetic part is linearly dependent on the baroreceptor firing rate, as shown in the following equation:

$$T_p(n) = \frac{n(t)}{M}. \quad (4.28)$$

The sympathetic part is indirectly proportional to the baroreceptor firing rate and includes a time-delay τ_d . Studies have shown that this delay varies between 6 and 10 seconds and is not present in the parasympathetic ANS

[39]. Additionally, increased vagal activity has an inhibitory influence on the sympathetic firing rate and is included in the denominator with a damping factor β (see table 4.2).

$$T_s(n) = \frac{1 - n(t - \tau_d)/M + u(t)}{1 + \beta T_p(n)} \quad (4.29)$$

The function $u(t)$ describes the influence of the vestibulo-sympathetic system, which accounts for the change in body position. Instead of choosing a hyperbolic function as in the original work, $u(t)$ is set to zero for the simulations, since no changes from horizontal to upright position, and therefore no orthostatic stress is investigated in this work.

The Heart as effector of the ANS

Similar to the model by Seidel and Herzel, the cardiac noradrenaline concentration is modelled as an ordinary differential equation based on sympathetic activity [39]. The cardiac acetylcholine concentration is calculated analogously, with τ_{nor} and τ_{ach} chosen according to table 4.2:

$$\frac{dC_{nor}}{dt} = \frac{-C_{nor} + T_s}{\tau_{nor}}, \quad (4.30)$$

$$\frac{dC_{ach}}{dt} = \frac{-C_{ach} + T_p}{\tau_{ach}}. \quad (4.31)$$

In order to generate a new heartbeat, an IPFM model based on the neurotransmitter concentrations, two scaling factors M_s and M_c , as well as an intrinsic heart rate H_0 was developed. Each time φ passes 1, a new heartbeat is generated and the integrator is reset to zero. Without input from the ANS, for example through denervation, a heartbeat would be generated every $\frac{1}{H_0}$ seconds. The input function for the IPFM is defined as

$$\frac{d\varphi}{dt} = H_0(1 + M_s C_{nor} - M_p C_{ach}). \quad (4.32)$$

Standard model parameters

Most parameters, such as τ_S , τ_I , τ_L , k_S , k_I , k_L , and M are derived from animal experiments, others were estimated empirically [39].

Table 4.2: Table of model parameters, derived from mean values for healthy young subjects [39].

Parameter	Value	Parameter	Value
k_S	3.06	N	100
k_I	1.91	α	0.78
k_L	2.22	β	4.48
τ_S	0.6	τ_{nor}	0.72
τ_I	5.26	τ_{ach}	1.32
τ_L	250	M_s	0.99
τ_d	6.12	M_p	0.45
M	120	H_0	100 $\frac{1}{min}$

4.3.2 Model expansion

In order to close the loop from the IPFM-model to the baroreceptors, the previously presented model had to be further expanded and enhanced.

The arterial Windkessel

In order to generate a blood pressure curve based on the the output of the IPFM model, which can then be used as an input for the baroreceptor sub-model, a three-element windkessel was chosen. Compared to its two-element counterpart, which is only based on the total arterial compliance C and the peripheral resistance R , this model gives a better relation between flow and pressure in the aorta by adding a term for aortic input impedance and depicts a more realistic total wavelshape. The impedance is denoted as R_c and accounts for the wave travel aspects, since it equals wave speed times blood density divided by aortic cross-sectional area [55]. The electrical analogon of the three-element windkessel is depicted in figure 4.4. It can be rewritten as:

$$p(t) = Z_c q(t) + p_{WK}(t) + P_\infty. \quad (4.33)$$

The arterial pressure $p(t)$ satisfies the following differential equation.

$$\frac{dp_{WK}}{dt} = \frac{1}{C_a} q - \frac{1}{R_p C_a} p_{WK} \quad (4.34)$$

P_∞ denotes the standard pressure in the system, which results in an initial pressure of $p_{WK}(0) = p(0) - P_\infty$. In order to solve the differential equation, a function for the flow from the aortic root $q(t)$ is needed [38]. It is was chosen based on findings in [42] as

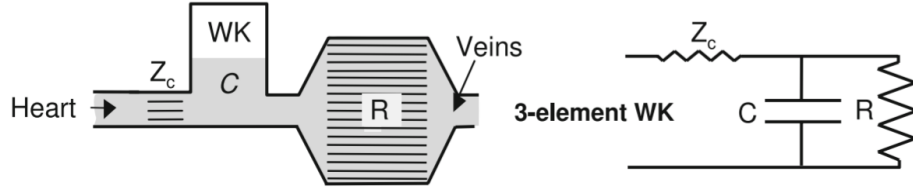


Figure 4.4: The three-element windkessel model as a part of the cardiovascular system and as electrical circuit [55]

$$q(t) = \exp\left(2\left(1 - \frac{1}{t_s}\right) + \frac{1}{\left(\frac{2t}{t_s-1}\right)^2 - 1}\right) \frac{SV}{I} \quad (4.35)$$

The systole duration in milliseconds is denoted as t_s , SV is the stroke volume in milliliters and I equals the integral of the exponential term in $q(t)$ over the interval $[0; t_s]$ [42]. This way, the total flow from the aortic root during the systole equals SV .

The findings by Boudoulas et al. were used to estimate t_s for different heart rates [11]. They performed minimally stressful diagnostic tests on 20 males and 20 females, all without a history of cardiovascular diseases. It was shown that a strong linear correlation between heart rate and systolic duration exists [11]. According to their results, the following linear function gives a sufficiently accurate description of the relation between the two:

$$t_s = 540 - 2.1 \cdot HR. \quad (4.36)$$

Stroke volume

The higher the heart rate, the smaller the ejected stroke volume. This physiological phenomenon was included into the existing model analogously to the approach presented by van de Vooren et al. [53] (see figure 4.5). The stroke volume V_{ref} at 60bpm was assumed to be 70ml and it was increased or decreased depending on the preceding RR-interval in milliseconds [8]. For the computation of the stroke volume of the n -th heartbeat SV_n , a left ventricle filling factor δ_n was introduced according to the following equation:

$$\delta_n = 0.5 + 0.5 \frac{RR_{n-1}}{1000}, \quad (4.37)$$

$$SV_n = \delta_n V_{ref}. \quad (4.38)$$

4.3. MODEL 3: AN HRV MODEL WITH DIFFERENT BARORECEPTOR TYPES 47

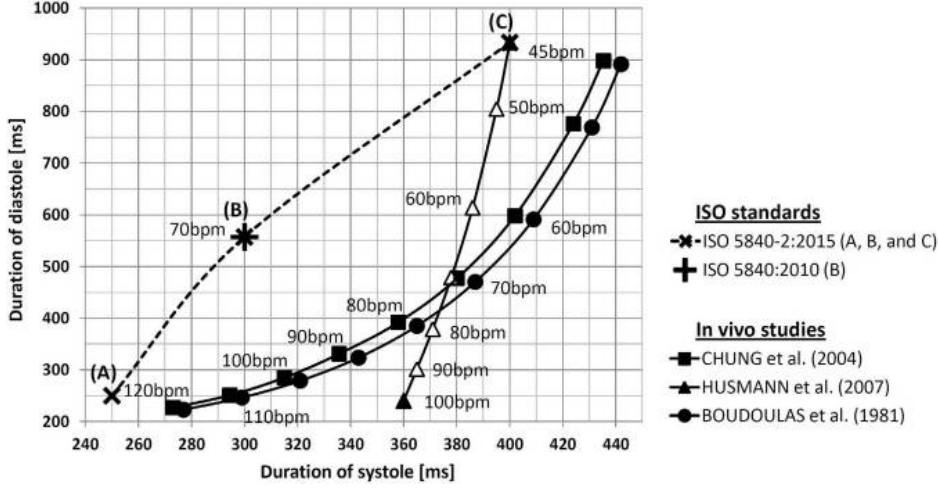


Figure 4.5: Relation between systolic duration, heart rate, and diastolic duration according to [8].

Autonomic nervous system activity

Since models for ANS activity usually include a basic oscillating sympathetic and parasympathetic activity, and are not only dependent on the firing rate of the baroreceptors, two sinusoidal functions with typical frequencies f_p and f_s were added to $T_p(n)$ (equation 4.28), and $T_s(n)$ (equation 4.29). This results in the following two equations:

$$T_p(n) = \frac{n(t)}{M} + C_p \sin(2\pi f_p), \quad (4.39)$$

$$T_s(n) = \frac{1 - \frac{n(t-\tau_d)}{M} + u(t)}{1 + \beta \frac{n(t)}{M}} + C_s \sin(2\pi f_s). \quad (4.40)$$

In order to avoid fast fluctuations in sympathetic nervous system activity, which could occur due to its linear dependence on the baroreceptor input, and dependency on the parasympathetic activity in the denominator of the first summand, a butterworth filter of order 3 and passband edge frequency of $0.15 \cdot 2\pi$ was applied to $T_s(n)$.

IPFM and Respiration

The input of the IPFM model was scaled with a function $\frac{1}{m(t)}$, which was chosen analogously to the one presented for the second model in equation 4.19 as the mean IPFM input over the last 10 seconds.

Different to the previously presented models, the respiration was included in model 3 by using a varying threshold for the IPFM, as proposed by Barbi et al [6]. Assuming that $r(t)$ is a continuous function, oscillating between -1, which equals total expiration, and 1, equalling total inspiration, the threshold $i(t)$ for the IPFM model is not held constant, but chosen as

$$i(t) = 1 + \frac{r(t)}{20} \quad (4.41)$$

4.4 Simulation

All three simulations were implemented in Simulink 2017b. From there, a vector containing the series of simulated RR-intervals is transferred to the Matlab 2017b workspace for further analysis.

RR-interval data from 30 subjects with essential hypertension was used to derive parameters for the simulation. Their main characteristics are summarised in table 4.3.

Slow breathing exercises were carried out in a sitting position, allowing abdominal breathing in the most uniform way. Inhalation and exhalation were guided by a balloon shown on a screen, which rises and sinks, animating the subject to breath in and out accordingly. One of six different breathing patterns was used for each subject, in order to create slow and even breathing without overstraining the subject (see figure 4.6). During the 10min breathing exercise, an ECG was recorded at a sampling rate of 256 Hz [4].

Table 4.3: This table shows the mean baseline characteristics and their standard deviation for the 30 subjects.

Age (years)	62.9 (7.7)
Gender	11 females / 19 males
Body height (cm)	174.4 (10.4)
Body weight (kg)	87.6 (18.9)
BMI	28.6 (4.7)
Arterial Hypertension since (years)	11.4 (10.2)
Systolic blood pressure (mmHg)	133.0 (17.1)
Diastolic blood pressure (mmHg)	83.8 (10.6)
Spontaneous breathing rate (1/min)	13.6 (1.9)

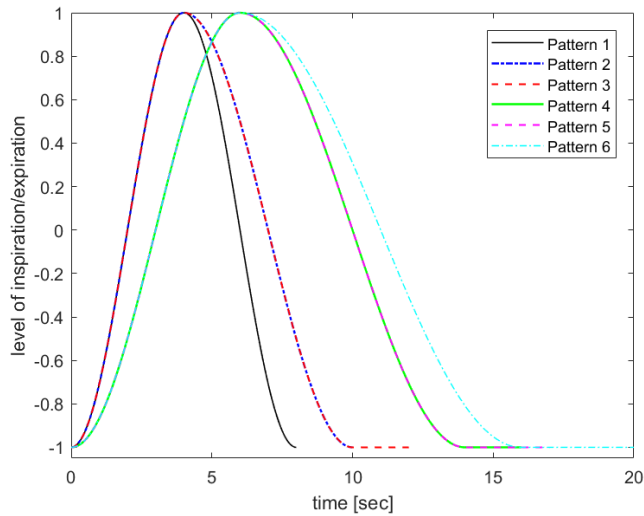


Figure 4.6: The prescribed respiratory patterns, with complete exhalation at -1 and complete inhalation at 1 .

As the standard duration for short-term HRV recordings is 5min [30], the 10min were split into two 5min recordings and hence 60 different data sets were used as basis for the simulation runs of each model.

The mean RR-interval \overline{RR} is easily derived from the sequence of a patients RR-intervals. For Model 1 and Model 2, T_0 was set to \overline{RR} and in case of Model 3 $H_0 = \frac{1}{\overline{RR}}$ (compare equations 4.10 and 4.32). Due to motion and other artifacts, the sequence of recorded RR-intervals contained a few Not-a-Number (NaN) entries, the same number of corresponding simulation output entries was randomly set to NaN.

For every model, the frequency components of the autonomic nervous system were determined, based on the analysis of the 5-min RR-interval recording in the frequency domain and the prescribed breathing pattern. As the ANS activity in the first model is exclusively dependent on the respiratory frequency f_r (compare equation 4.3 and 4.4), a periodic function $f_r(t)$, representing the respective prescribed breathing pattern, was chosen. Instead of having a standard sine function, a periodic function with period length of 8 to 20 seconds was designed. In order to maintain the amplitude of a sine function, complete exhalation was specified as -1 and complete inhalation as 1 analogously. The six different functions for the prescribed breathing patterns are shown in figure 4.6 for one breathing cycle. During inspiration and expiration, they follow a sinusoidal course, respectively. Patterns 4 to 6 also include a phase of sustained complete exhalation before the next breathing cycle starts.

For model 2 and 3, frequencies for the sympathetic and the parasympathetic branch of the ANS need to be determined. Therefore, a Lomb-Scargle periodogram of the patients RR-intervals is calculated. The sympathetic frequency is chosen as the frequency with the highest power in the interval from 0 – 0.15 Hz. The same applies for the parasympathetic activity and the frequency band from 0.15 – 0.4 Hz.

For the solution of the various non-stiff differential equations, the `ode45` solver with variable step size was used. It uses an explicit Runge-Kutta(4, 5) formula, the Dormand-Prince pair [44].

Every simulation was performed for 1000 seconds, from which only the last 300 seconds were selected for further statistical analysis. This allows the whole system to reach a stable state. The statistical analysis was performed as described in chapter 3.1 and 3.2. The Lilliefors and the Wilcoxon signed rank test were performed with the pre-implemented Matlab functions `lillietest` and `signrank`.

5 Results

In the course of the following chapter, the main simulation results are described and depicted for all three models. SDNN, SDDSD, RMSSD, SD1, SD2, as well as Poincaré plots are analysed. For further statistical assessment, the Lilliefors and the Wilcoxon signed rank test are applied.

5.1 Poincaré Plots

The Poincaré plots of the first models 60 simulation runs clearly show a tendency of overestimation of the mean heart rate, equalling an underestimation of mean RR-interval length. This is apparent through the shift of the whole set of points along the line of identity, compared to the given patient data, which is visibly detectable without the need for further statistical quantification at this point (see figure 5.1).

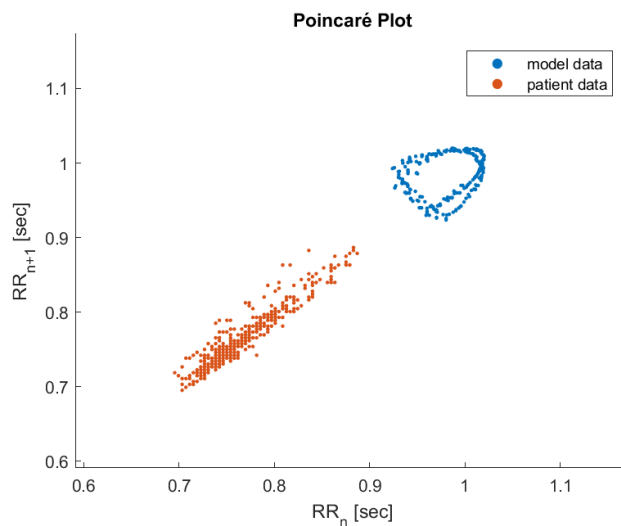


Figure 5.1: Model 1: Poincaré plot of the first 5min recording of subject number 8, with corresponding simulation output.

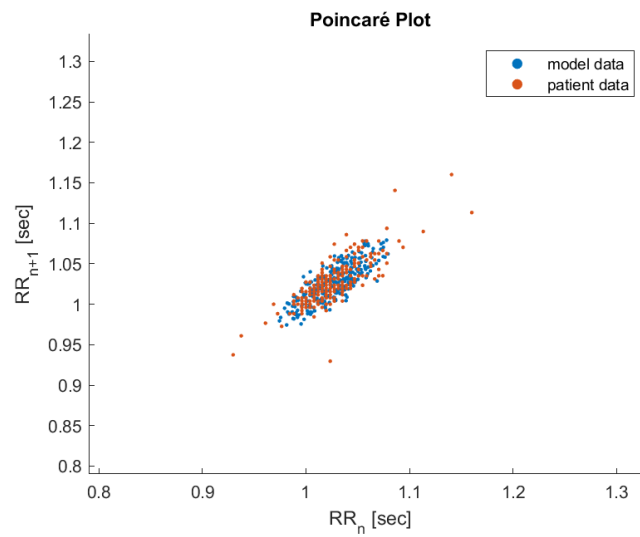


Figure 5.2: Model 2: Poincaré plot of the first 5min recording of subject number 23, with corresponding simulation output.

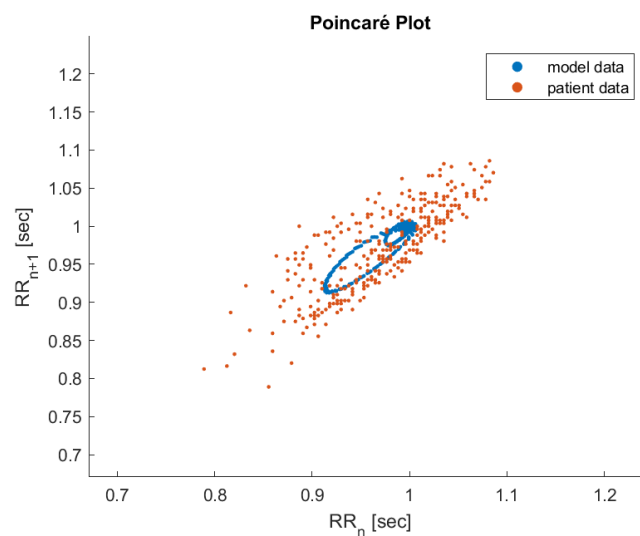


Figure 5.3: Model 2: Poincaré plot of the first 5min recording of subject number 25, with corresponding simulation output.

Another significant mismatch between given data and simulated data lies in the general shape of the point cloud. As presented in figure 3.2, a typical distribution of points has a comet-like shape, whereas the simulated data presents itself in a more circular shape without any points in the centre of

the point cloud.

For the second model, in general a considerably better Poincaré plot could be achieved, especially in relation to the mean heart rate. As shown in figure 5.2, the two point clouds appear mostly overlapping, aside from the outliers of the patient data. For some cases however, the simulation output resulted in an atypical, elliptically appearing line, rather than a comet-like cloud of points (figure 5.3). This phenomenon occurred mostly in connection with input data, showing a rather large general dispersion of points.

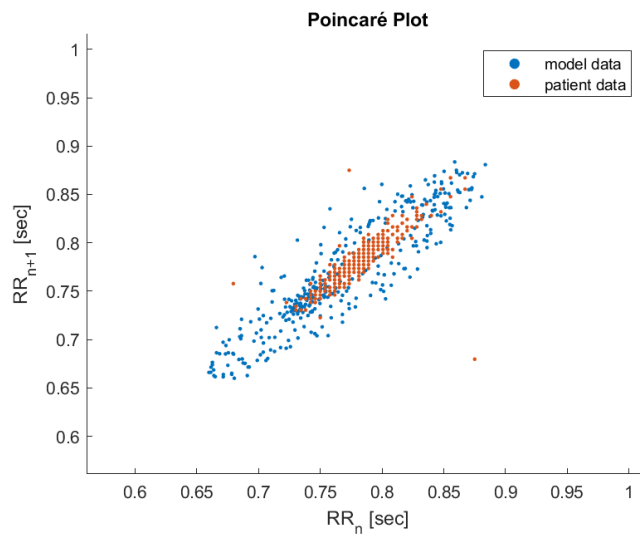


Figure 5.4: Model 3: Poincaré plot of the first 5min recording of subject number 20, with corresponding simulation output.

The third model showed similar results concerning the mean heart rate, but a tendency of overestimation of the plots length and width was observed. For a variety of data sets, the plot showed a lack of points in the centre of the point cloud, although far less pronounced in comparison to the first model 5.4. In contrast, for 7 of the 60 simulation runs, the output of the third model was similar to the one by model 2 depicted in figure 5.3.

5.2 Statistical HRV Analysis

Six statistical parameters were used for the quantification of the RR-data: mean RR-duration, SDD, SD1, SD2, SDNN, and RMSSD.

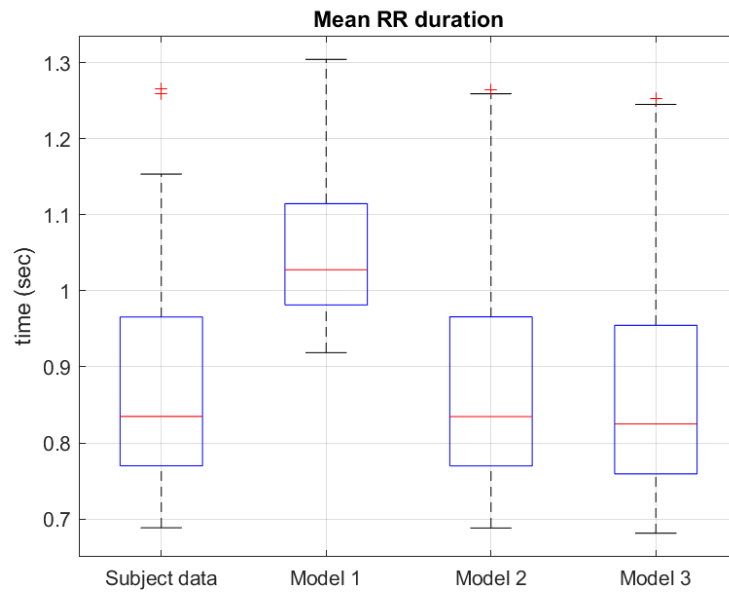


Figure 5.5: Boxplot of mean RR intervals of the subject data and all three models.

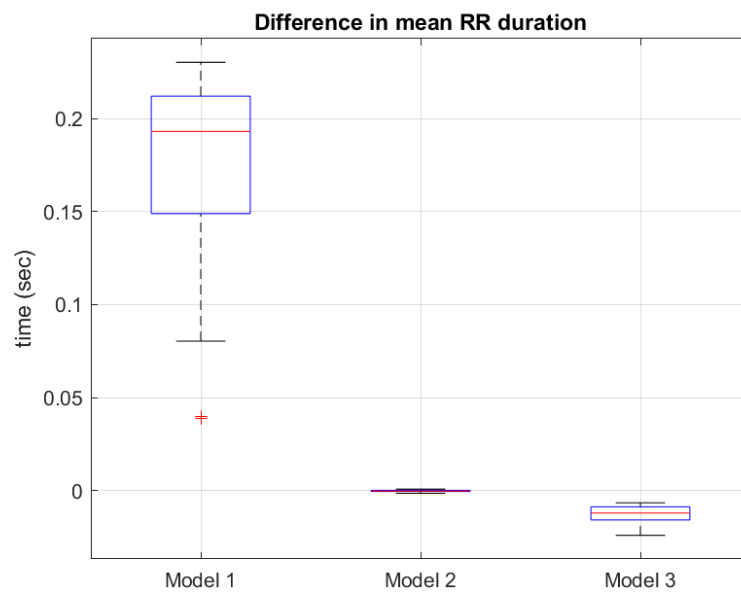


Figure 5.6: Boxplot of differences of mean RR intervals between subject data and each of the three models.

As the Poincaré plot in the last section already indicates, model 1 tends to overestimate the RR-interval length drastically. This result is underpinned by the distribution of the mean RR-duration, which is summarised in figure 5.5. For model 2 and 3, a very good replication of mean RR-duration could be reached, as their boxplots are nearly identical to the subjects.

To prove that the 60 mean RR-durations from the simulation runs of model 2 and 3 do not only come close to those of the subjects as a group, but also individually, their difference to the patient data was calculated for every subject and again summarised in a boxplot (see figure 5.6). Again, the difference in mean RR-duration resulting from the first model is considerable, whereas model number 2 shows a practically perfect fit. A slight underestimation of the mean RR-duration by the third model becomes more obvious in this depiction, but the results still are close to the optimum of zero difference.

Analogous to this, boxplots of the other five statistical parameters and their differences to subject data were created and are shown in figure 5.7 and 5.8. The results for the SDDSD show a similar pattern to that of the mean RR-intervals. Again, the first model clearly overestimates the SDDSD, opposite to the second and third model, which show a considerably better fit. When looking at the differences it should be noted, that the second model shows a slight underestimation, whereas the third model overestimates the SDDSD a little.

SD1, the standard deviation along the X_1 axis (compare figure 3.2), which accounts for high frequency components, is a scaled version of the SDDSD according to equation 3.9 and therefore shows the same behaviour concerning the boxplot. The according overestimation of SD1 by the third model can also be observed in 5.4, as the model data deviates more from the line of identity in X_1 direction than the patient data. On the contrary, SD1 is slightly underestimated by the second model. The first model again shows the least satisfying results.

Analogously to SD1, SD2 equals the standard deviation along the X_2 axis. Model 1 and 2 show a comparable amount of underestimation, opposed to a considerable overestimation by model 3. Again this behaviour is also observable in the Poincaré plot in figure 5.4, as an overly long extension of the model data along the line of identity.

SDNN, which is a measure of total spectral power according to section 3.1.1, is most accurately represented by the output of the first model, slightly underestimated by the second model and clearly overestimated by the third.

The RMSSD, which reflects high frequency components (compare section 3.1.1), basically shows the same behaviour as the previously described SD1.

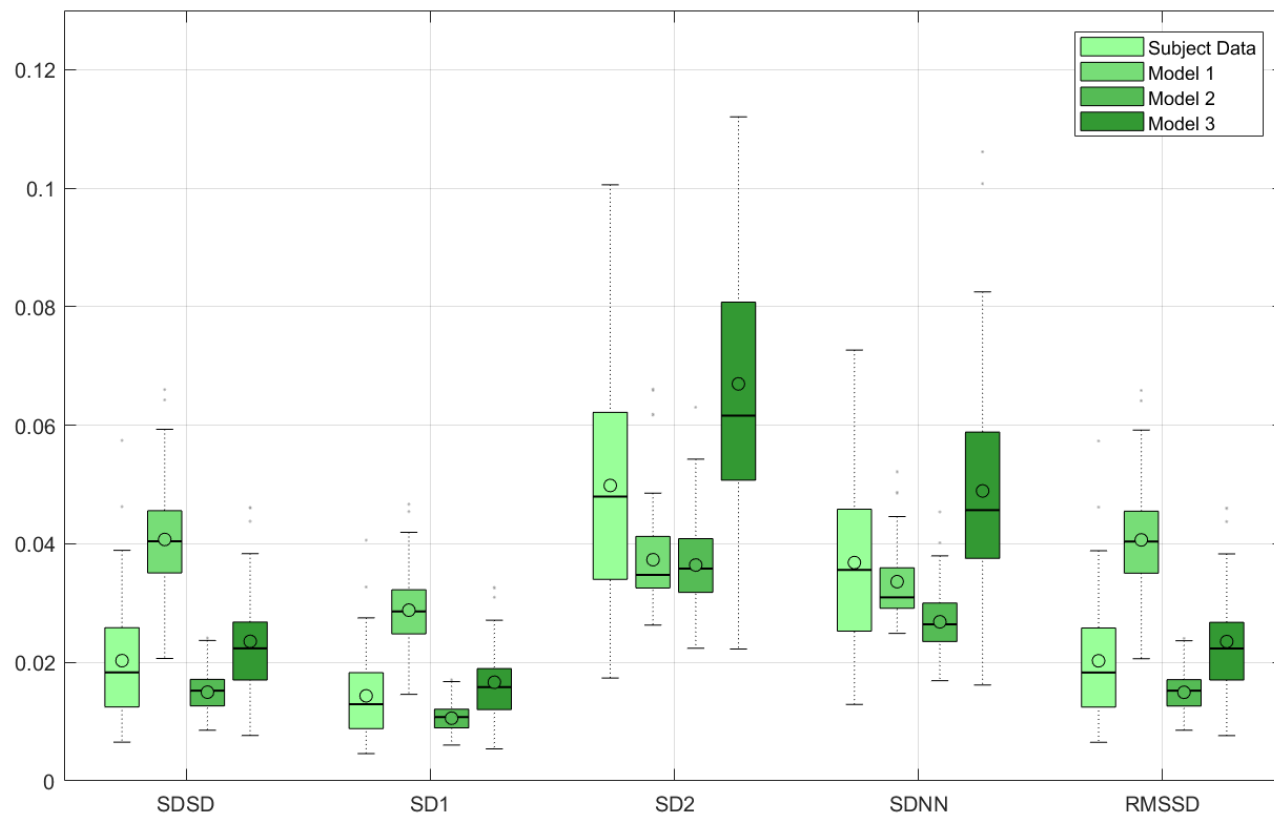


Figure 5.7: Boxplot of SDD, SD1, SD2, SDNN, and RMSSD of the subject data and all three models.

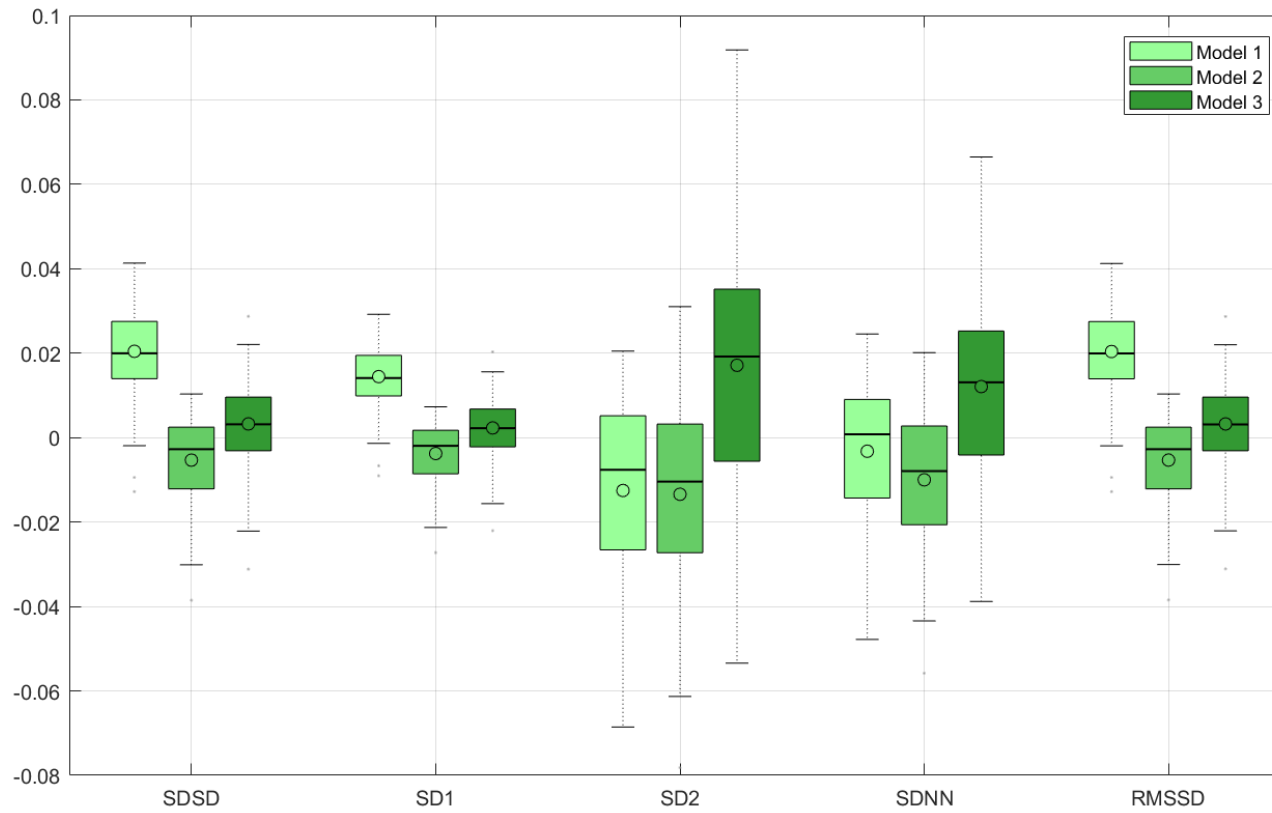


Figure 5.8: Boxplot of SDDSD, SD1, SD2, SDNN, and RMSSD differences between the subject data and each of the three models.

Table 5.1: Results of the Lilliefors Test applied to all statistical parameters derived from subject data and the three models. Results indicating the rejection of the null-hypothesis are marked grey.

	Subject Data	Model 1	Model 2	Model 3
mean RR	0.0082	0.0296	0.0074	0.0165
SDSD	0.0030	0.3171	0.5000	0.0393
SD1	0.0030	0.3171	0.5000	0.0393
SD2	0.0900	0.0010	0.5000	0.0134
SDNN	0.1368	0.0010	0.5000	0.0321
RMSSD	0.0030	0.3148	0.5000	0.0395

Table 5.2: Results of the Wilcoxon Signed Rank Test applied to all statistical parameters from all three models compared to the subject data. Results indicating the rejection of the null-hypothesis are marked grey.

	Model 1	Model 2	Model 3
mean RR	0	0.0031	0
SDSD	0	0.0015	0.0142
SD1	0	0.0015	0.0142
SD2	0.0002	0	0.0002
SDNN	0.2508	0	0.0002
RMSSD	0	0.0015	0.0139

The Lilliefors Test was applied to all the data sets, based on the null-hypothesis that each of them comes from a normal distribution. The results are summed up in table 5.1. Each time the null-hypothesis was rejected, the corresponding table entry was marked grey. Generally, no clear behaviour was identifiable for the test results.

In order to ensure comparability of the results, all further comparisons were performed with the non-parametric Wilcoxon Signed Rank test. The null-hypothesis of this test states, that the difference of the two data sets comes from a distribution with zero median. The results are summed up in table 5.2 and marked grey analogous to the previous test. It is apparent, that the SDNN in model 1 presents the only case in which the null-hypothesis is not rejected.

5.3 Blood Pressure

For Model 1 and 2, blood pressure showed a highly unusual behaviour for a remarkable number of cases. The systolic blood pressure never reached a value less than 140mmHg and the diastolic blood pressure never fell below 100mmHg on a noteworthy scale for all of the simulation runs of the first model. For the second model, systolic blood pressure reached values of up to 190mmHg, with diastolic pressure ranging from 80 to as high as 150mmHg. This behaviour has a severe impact on the sympathetic activity, which is mainly dependent on the blood pressure function and its first derivative (described in equation 4.2). It is clearly noticeable, that once systolic blood pressure levels exceed 160mmHg, sympathetic activity shows phases of zero activity or even vanishes completely. This absence of neuronal excitation was observable for 10 of the 60 simulation runs of model 1 and 26 of the simulation runs of model 2.

The effect of this is also apparent regarding the corresponding Poincaré plot. Figure 5.9 shows a typical distribution of model data points, resulting from absent sympathetic activity. The inexistence of the sympathetic oscillator activity results in a very regular pattern of the distribution of points, compared to 5.3 for example.

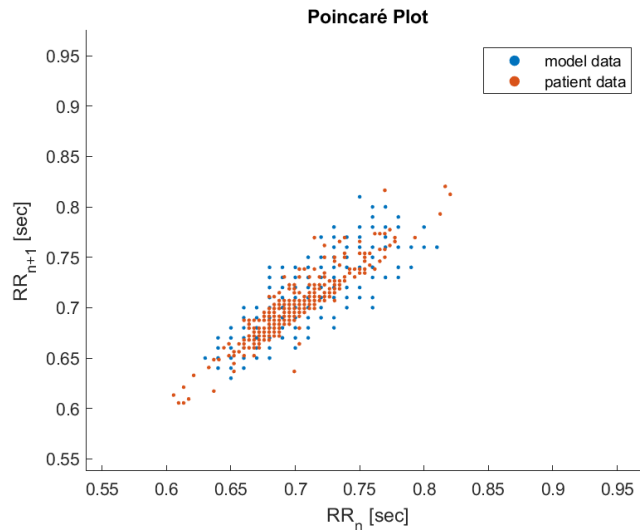


Figure 5.9: Typical distribution of data, coming from a simulation run of model 2 (subject 24, first 5min recording) with zero sympathetic activity, due to overestimated levels of blood pressure.

Another noteworthy result is the context of blood pressure and sympathetic activity are the rapid changes in systolic, as well as diastolic blood pressure, caused by sympathetic activity in the first and second model. Over the course of a few successive heartbeats, the systolic blood pressure varies by up to 20mmHg for both models, although less pronounced for the first than the second model (see figures 5.10 and 5.11). This is due to the impact of sympathetic nervous activity on the cardiac noradrenaline concentration, which influences contractility, and the vascular noradrenaline concentration, responsible for the windkessel time constant. Another cause of blood pressure fluctuations of about 10mmHg in both models is presented by respiratory activity. The changes in pressure are time-delayed in a way, that the peak in blood pressure appears shortly before a maximum level of inhalation is reached.

For the third model, blood pressure curves show a different behaviour. During none of the simulation runs, a systolic blood pressure higher than 130mmHg was reached, and it generally showed only small fluctuations (1-5mmHg) over time. For the diastolic blood pressure, values from 60-70mmHg were observed, with two exceptional cases of 40mmHg and 50mmHg. In contrast to the systolic blood pressure, diastolic values showed quick changes of up to 10mmHg over the course of only a few heartbeats, as shown in figure 5.12. Furthermore, the described diastolic variations showed a strong dependency on the parasympathetic influence on the IPFM.

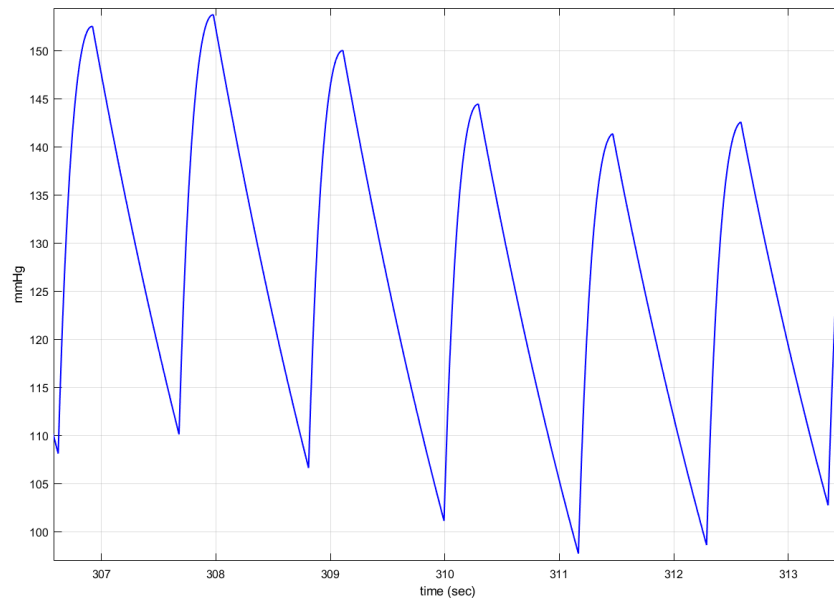


Figure 5.10: Blood pressure fluctuations of Model 1 (subject 2).

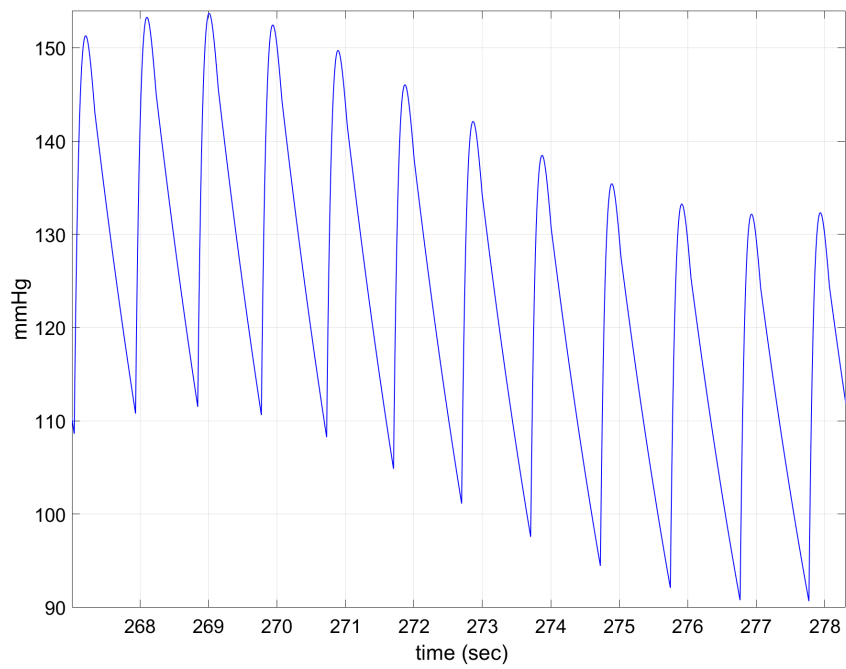


Figure 5.11: Blood pressure fluctuations of Model 2 (subject 2).

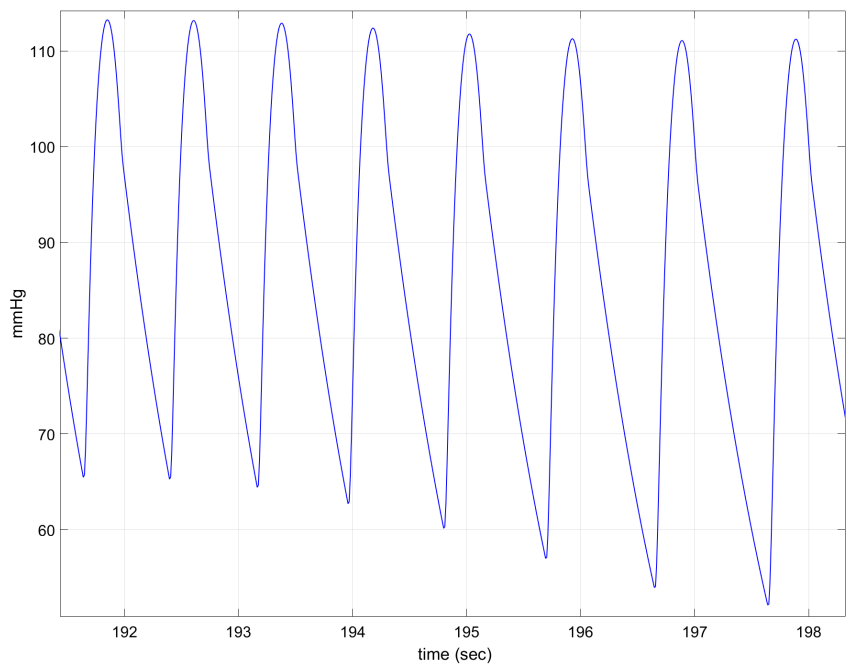


Figure 5.12: Blood pressure fluctuations of Model 3 (subject 3).

Another notable observation about the behaviour of the blood pressure is its dependence on respiration. For the third model, respiration is included via variation of the IPFM threshold. It has an instantaneous influence on the occurrence time of the next heart beat, and consequently on blood pressure. For the first and second model, blood pressure variations can be observed, but due to the fact that respiration is included into the models ANS part, the time delay in sympathetic and parasympathetic activity results in a time delay between respiration and blood pressure variations.

6 Discussion

In this chapter, the previously presented simulation outcomes are discussed in greater detail, allowing a broad comparison of the overall model performances. Their advantages and insufficiencies are addressed, in order to point out further possibilities for model improvement and expansion.

The Integral Pulse Frequency Modulation Model

The first and most obvious result was the significant overestimation of the mean heart rate by the first model. This may be due to the fact that, although IPFM models are widely used in literature (see section 2.3), their input functions are often designed to mimic physiological processes, but not further mathematically analysed. The IPFM input should equal 1 over the whole simulation run, in order to correctly recreate the mean heart rate. Meste et al. state, that the problem of selecting an adequate model input is not usually addressed when using an IPFM model, and respiration is widely neglected as an input, because it is not simply representable by a cosine function [36]. Although the focus of most models clearly lies more on the correct representation of heart rate variability than on mean heart rate, they are both interdependent and show an inverse correlation. The faster the mean heart rate is, the less room there is for variations, and therefore mean heart rate should be additionally considered when modeling heart rate variability [2].

The original version of the third model showed a similarly false behaviour when it comes to the mean heart rate. For the second and third model, the introduction of a function rescaling the IPFM input based on the mean function value over the last 10 seconds (equation 4.19) did indeed improve the results considerably, but this approach does not address the root of the problem. A look at the corresponding boxplots in figure 5.5 and 5.6 shows remarkable improvement of the mean heart rate, especially for the second model. The third model also shows only a minimal underestimation of the heart rate.

Still, if the mean amplitude of the IPFM model input is, for example, too low, and therefore upscaled, the amplitude of the periodic input components is also increased, instead of simply raising the level of activity by a constant value and holding the amplitude of the periodic components constant. Moreover, the low frequency input signal components, especially those with a period length of over 10 seconds, are dampened by this kind of signal modification. This indirectly excludes the ultra low frequency components of HRV, which is not a problem regarding short term HRV, but it makes the approach unsuitable for use in modeling and simulation of HRV over longer periods of time, such as 24h.

The change in amplitude of periodic signal parts has notable effects on the shape of the Poincaré plot and the measures of HRV. For the third model, the input of the IPFM was generally underestimated. By upscaling it, fluctuations of the incoming signal were reinforced, resulting in a greater overall variability. This is evident in the Poincaré plot in figure 5.4, where the general plot shape looks rather decent, but shows too much expansion in every direction. Consequently, all of the measures for HRV, as depicted in figure 5.7, are too high compared to subject data. The exact opposite behaviour is observable for the second model.

The Baroreceptors

Seidel and Herzel already address the problem of adequately modeling baroreceptor activity in their work. They state, that it is not reasonable to put much effort into modeling one element of the system [43]. Not aiming to recreate reality in all its richness of detail is indeed a cornerstone of model design, but if all following model equations build on the activity of the baroreceptors, a more detailed approach would clearly be desirable at this point. Although baroreceptors can be loosely thought of as controllers, which react proportionally and differentially to changes in blood pressure (compare equation (4.2)), a multitude of other characteristics was consciously ignored in their model. Those include adaption to changes in mean pressure, saturation at high pressure, dependence on the trend of the pressure change, different types of baroreceptors, and conduction times to the medulla. They further state that improvements were reasonable, if the physiology of the medulla was better understood [43], but basic baroreceptor characteristics, such as the adaption to mean pressure levels should be included, despite incomplete knowledge of neuronal mechanisms in the brain stem. DeBoer et al. for example used a scaled arctangent function to mimic saturation at high and low pressure levels, which does not add an unnecessary amount of complexity to the model, but still mimics the nervous reaction to blood

pressure changes much more accurately [20].

For the third model, three different types of baroreceptors were presented, in order to account for the variation in thresholds for different baroreceptor types. They also include a maximum firing rate, which is without doubt a reasonable and necessary assumption, since the firing rate is generally limited by the duration of the absolute refractory phase of baroreceptor ion channels. Their dependency on mean blood pressure over the last 1, 5, or 250 seconds gives them an adaptability to longer phases of, eg., hypertension, which is clearly missing in the first model [39]. Moreover, this modeling approach still presents an easily implementable, yet physiologically much more accurate basis for the input of the autonomic nervous system, since at least two different types of baroreceptors are known [29]. Potential future models should at least include the main characteristics of baroreceptor physiology. A modeling approach on a cellular level, including ion channel dynamics, might be worth implementing, in order to gain a better understand of the physiological regulatory mechanisms.

ANS Activity

The first model includes the basic characteristics of sympathetic and parasympathetic activity. They both show an oscillating behaviour and are modulated by baroreceptor activity, giving them a seemingly antagonistic behaviour. The basic frequency of both branches of the ANS was set equal to the respiratory frequency, which is contrary to the fact, that respiratory changes in heart rate were shown to be modulated mainly by parasympathetic activity [23]. The first model also modulates sympathetic activity proportional to the current baroreceptor activity, which is an assumption incompatible to the fact, that sympathetic activity is widely attributed to the low frequency components of HRV [30]. The erroneous regulation of sympathetic activity proportional to baroreceptor activity is also evident, if one considers that a maximum function had to be included into the model in equation 4.3, in order to prevent negative sympathetic activity values. Another shortcoming lies in the complete absence of autonomous ANS activity independent from modulating factors.

The identified shortcomings of the first model were addressed in the second model via inclusion of two oscillators for fundamental ANS activity, a low pass filter for sympathetic activity, and the inclusion of respiration only in the parasympathetic part of the model. The simulation results were superior to those of the first one by far, but still undesirable phases of zero sympathetic activity occurred, resulting in a lack of HRV as depicted in figure 5.9. This leads to the conclusion, that baroreceptor activity and respiratory

influences should not be included directly into sympathetic activity, if one locates sympathetic activity in the low frequency spectrum.

For the third model, the absence of independent ANS activity was analogously evened out by the inclusion of two oscillators. Since sympathetic activity was again directly dependent on the baroreceptor firing rate, another low pass filter was included. This causes a reaction to quick changes in blood pressure mainly mediated via the parasympathetic nervous system, which is consistent since this ANS part is attributed to the high frequency components of HRV. A positive aspect of the third model is the direct dependence of sympathetic on parasympathetic activity, accounting for their typical antagonistic behaviour.

Respiration

Respiration, as a main influence on short term HRV, was included into the models in two different ways: The first and second model include respiration in the central nervous system, which is comprehensible, since changes in parasympathetic activity exist due to central modulation of respiration [23]. A disadvantage of this technique lies in the resulting temporal shift between inspiration and augmentation of the heart rate.

The third model avoids this type of shift by varying the IPFM threshold based on the current level of in- and exhalation, leading to an instantaneous change of heart rate. An overestimated level of change in threshold may also account for the overestimation of short term variability by the third model and could be probably further improved.

It still is questionable, whether respiratory sinus arrhythmia should be modelled via the parasympathetic nervous system, or directly influence heart rate.

Blood Pressure

Effective blood pressure regulation serves as an indicator of how well the model is constructed, since controlling mechanisms such as the baroreceptor reflex do regulate the heart rate with the aim of keeping blood pressure levels within a normal range. In Studies, systolic blood pressure was shown to increase during phases of exercise and higher heart rate, whereas diastolic blood pressure was only slightly augmented in all age groups and for all heart rates [37]. The first and second model show significant changes in systolic, as well as diastolic blood pressure. Additionally, overestimated average blood pressure levels cause the previously mentioned phases of zero sympathetic

activity. This is clearly not a desirable outcome and can be attributed to a combination of inadequacies. Quick changes in blood pressure during systole are normally evened out by the windkessel effect of the aorta. Although the first and second model do include a windkessel time constant, it only effects the diastolic pressure decrease. During systole, only the contractility varies based on sympathetic activity. This combination results in overly high blood pressure levels. Also, stroke volume and its dependence on the heart rate was not included, which further increases blood pressure levels.

In comparison to the first two models, the third one showed a very stable mean systolic blood pressure for all patients and all mean heart rates, whereas the diastolic pressure showed fluctuations. The model expansion including heart rate dependent stroke volume and an arterial windkessel, clearly had a stabilising effect on blood pressure. Especially the windkessel regulates blood pressure during systole, as well as diastole, and gives a more physiologic shape to the pressure curve. Although the third model behaves more realistic than the other two, correct selection of compliance and resistance is essential for an accurate calculation of blood pressure. Furthermore, fluctuations in rapid changes in diastolic blood pressure should be avoided generally. What is missing in the third model, is not only stroke volume, but also contractility depending on the filling of the heart, as described by the Frank-Starling-Mechanism. Varying peripheral resistance over time also presents a possibility for further model extension.

Further Remarks

In principle, the third model also includes the option of taking posture into account via the input from the vestibulo-sympathetic system. This presents another possibility for model expansion beyond the autonomic system.

Moreover, it is still not clear whether guided respiration differs from spontaneous respiration in its effect on the heart rate.

Another point worth mentioning is that higher levels of sympathetic activity also lead to decreased oscillations, generating a rather metronomic heart rate, as found in patients suffering from burn-out [15].

The results of the Lilliefors test in table 5.1 display an irregular pattern, concerning the rejection of the null-hypothesis that a dataset comes from a normal distribution. According to the results of the Wilcoxon Signed Rank test in table 5.2, the null-hypothesis has to be rejected for all but one case. This means that one cannot assume that the difference between two data sets comes from a distribution with zero median in a majority of cases. Although the models were designed as close to reality as possible, this indicates that significant statistical differences do exist. Consequently, there is still enough

room for further improvements.

Limitations

Although the presented models do include the most important effectors of the heart rate, other factors still need to be included for further improvement. The most obvious features of the human body, such as age and gender, are remarkably uncommon in modeling and simulation of the cardiovascular system, although they do play a notable role (compare subsection 2.1.3). Especially the age-dependent reactivity of the baroreceptors should be taken into account.

Not only baroreceptors, but also chemoreceptors control the activity of the autonomous nervous system, since they transmit information about the current oxygen supply to the respiratory centre of the autonomous nervous system [46].

Posture also plays a role in heart rate regulation, due to the fact that the autonomous nervous system has to counteract gravity, when changing from a horizontal to a vertical position. The vestibulo-sympathetic system was already included into a model by Olufsen et al. [39], but should still be further investigated.

A very central, but still largely unmodelled part of the cardiovascular regulators is the medulla, which is probably due to the complexity of neuronal interplay in the brain stem and the difficulty of examining it clinically. Once mathematically accurate descriptions of the regulatory mechanisms in the medulla exist, they should without doubt be included into models for HRV. If an HRV model should be suitable for simulation over longer periods of time, ultra low frequency components, eg., circadian rhythms, need to be included into the model [31].

6.1 Conclusion

The research questions posed in section 1.2. shall now be addressed once again.

Although lots of existing models and submodels of the cardiovascular system already include a variety of regulatory mechanisms of the HRV, they reveal shortcomings when closer examined. A lot of them do not address physiological processes in detail, or are largely based on purely statistical evaluations. The first implemented model includes a variety of regulatory mechanisms, such as baroreceptors, sympathetic and parasympathetic activity, cardiac as well as vascular noradrenaline concentration, a windkessel time constant, and myocardial contractility. Despite the many regulatory mechanisms it failed to mimic even the mean heart rate of the given subject data correctly, as the input of the IPFM was not closer examined.

The second model, which resulted from enhancements based on medical considerations of the first one, showed significant improvements in model performance when compared to subject data. However, it still generates physiologically untenable outputs for some cases. Phases of zero sympathetic activity caused by poor modeling of the baroreceptors, high fluctuations in systolic and diastolic blood pressure, and an incomplete arterial windkessel still provide starting points for further model enhancements.

The third model, being a combination of physiologically well-founded models, includes a more accurate description of the baroreceptors, and was also extended to further enhance its performance. Nevertheless, it overestimates short term as well as long term variability, which may be due to an inadequate choice of input for the IPFM model. In order to adequately recreate the mean heart rate given by the subject data, the IPFM input had to be evened out by a correction term analogously to the one used for the second model.

In summary, models of cardiovascular regulation with an emphasis of correct representation of heart rate variability do exist, but only some of them are able to mimic reality to a satisfying degree. Modeling approaches, although physiologically valid, often put an emphasis on single aspects of the cardiovascular system, and simultaneously neglect others, which leads to a limited function of the whole model.

Once the existing regulatory mechanisms are accurately modelled, further enhancements may include age, gender, chemoreceptors, posture, hormonal regulation or even parts of the central nervous system. Nevertheless, further research needs to find a balance between a models richness of detail and an excessive amount of uncertain parameters.

7 Appendix

The appendix includes images of the model implementations in Simulink 2017b.

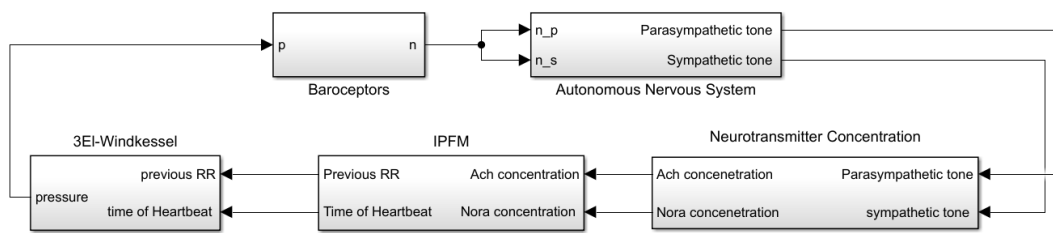


Figure 7.1: Simulink implementation of Model 3.

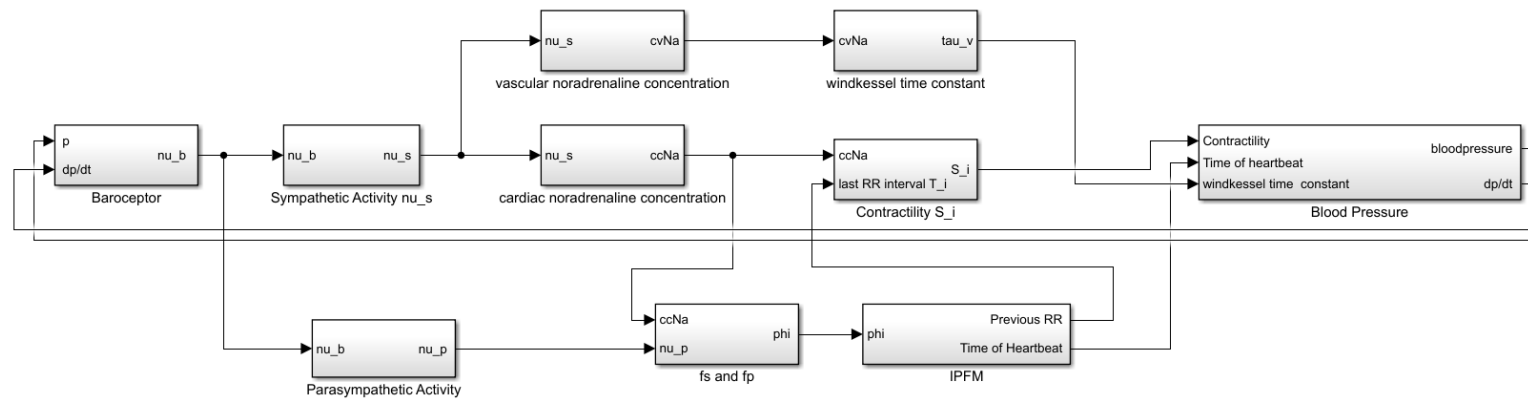


Figure 7.2: Simulink implementation of Model 1 and 2.

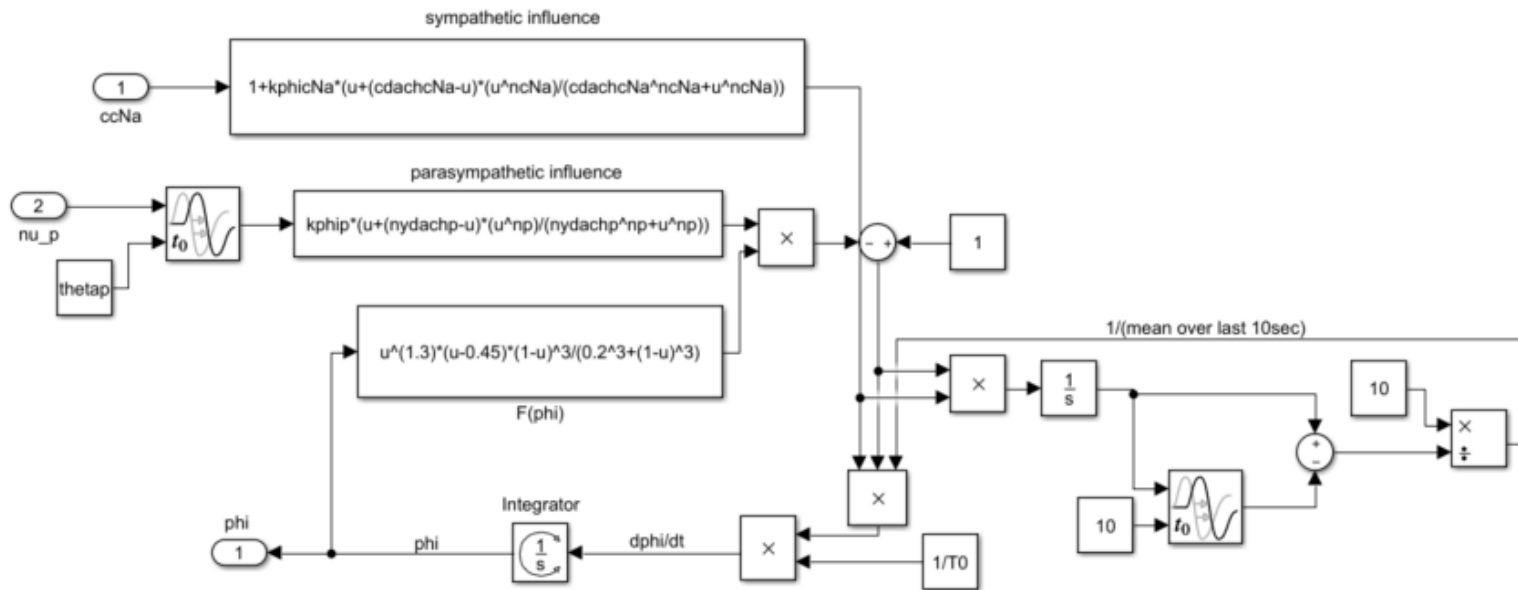


Figure 7.3: Implementation of the IPFM model in Model 2. Aside from the calculation of the mean over the last 10 seconds (visible on the right), it is equivalent to the IPFM model in Model 1.

List of Figures

1.1	Causes of death in Austria in 2014	2
2.1	Circulation of blood through the heart	6
2.2	Heart Cycle	7
2.3	Sympathetic and parasympathetic nerves of the heart	10
2.4	Sinus node depolarisation	11
2.5	Atrial pressure and ANS	12
2.6	Simulation Circle	18
3.1	Schematic representation of an ECG recording	24
3.2	Poincaré Plot	27
4.1	Seidel schamatic model representation	34
4.2	The phase effectiveness curve.	37
4.3	Olufsen schamatic model representation	42
4.4	3-element Windkessel	46
4.5	Systolic duration and heart rate	47
4.6	Respiration Patterns	49
5.1	Exemplary Poincaré Plot Model 1	51
5.2	Exemplary Poincaré Plot Model 2 Nr 1	52
5.3	Exemplary Poincaré Plot Model 2 Nr 2	52
5.4	Exemplary Poincaré Plot Model 3	53
5.5	Boxplot of mean RR intervals	54
5.6	Boxplot of differences of mean RR intervals	54
5.7	Boxplot of SDD, SD1, SD2, SDNN and RMSSD	56
5.8	Boxplot of SDD, SD1, SD2, SDNN, and RMSSD differences	57
5.9	Exemplary Poincaré Plot without Sympathetic Activity	59
5.10	Blood Pressure Model 1	60
5.11	Blood Pressure Model 2	61
5.12	Blood Pressure Model 3	61

7.1	Simulink implementation of Model 3.	71
7.2	Depiction of the Simulink implementation of Model 1 and 2	72
7.3	IPFM Model of Model 2	73

List of Tables

4.1	Table of standard parameter set of model by Seidel and Herzel [43].	38
4.2	Table of model parameters for model 3	45
4.3	Summary of subject data	48
5.1	Lilliefors test results	58
5.2	Wilcoxon signed rank test results	58

Bibliography

- [1] U Rajendra Acharya, K Paul Joseph, Natarajan Kannathal, Lim Choo Min, and Jasjit S Suri. Heart rate variability. In *Advances in cardiac signal processing*, pages 121–165. 2007.
- [2] Ivana Antelmi, Rogério Silva De Paula, Alexandre R Shinzato, Clóvis Araújo Peres, Alfredo José Mansur, and Cesar José Grupi. Influence of age, gender, body mass index, and functional capacity on heart rate variability in a cohort of subjects without heart disease. *The American journal of cardiology*, 93(3):381–385, 2004.
- [3] Benhur Aysin and Elif Aysin. Effect of respiration in heart rate variability (HRV) analysis. In *Engineering in medicine and biology society, 2006. EMBS'06. 28th annual international conference of the IEEE*, pages 1776–1779. IEEE, 2006.
- [4] Martin Bachler, Walter Sehnert, Ines Mikisek, Thomas Mengden, and Siegfried Wassertheurer. Abstract 15861: Device-guided slow breathing with real-time biofeedback for personalized cardiovascular therapy support increases pulse transit time. *Circulation*, Vol 138, 2018.
- [5] Raquel Bailón, Ghailen Laouini, César Grao, Michele Orini, Pablo Laguna, and Olivier Meste. The integral pulse frequency modulation model with time-varying threshold: application to heart rate variability analysis during exercise stress testing. *IEEE transactions on biomedical engineering*, 58(3):642–652, 2011.
- [6] Michele Barbi, Santi Chillemi, A Di Garbo, Rita Balocchi, and D Menicucci. A minimal model for the respiratory sinus arrhythmia. *Biological cybernetics*, 94(3):225–232, 2006.
- [7] Riccardo Barbieri, Eric C Matten, AbdulRasheed A Alabi, and Emery N Brown. A point-process model of human heartbeat intervals: new definitions of heart rate and heart rate variability. *American*

Journal of Physiology-Heart and Circulatory Physiology,
288(1):H424–H435, 2005.

- [8] Ovandir Bazan and Jayme Pinto Ortiz. Duration of systole and diastole for hydrodynamic testing of prosthetic heart valves: Comparison between iso 5840 standards and in vivo studies. *Brazilian journal of cardiovascular surgery*, 31(2):171–173, 2016.
- [9] Gary G Berntson, John T Cacioppo, and Karen S Quigley. Respiratory sinus arrhythmia: autonomic origins, physiological mechanisms, and psychophysiological implications. *Psychophysiology*, 30(2):183–196, 1993.
- [10] Bernadette Biondi, Emiliano A Palmieri, Gaetano Lombardi, and Serafino Fazio. Effects of thyroid hormone on cardiac function—the relative importance of heart rate, loading conditions, and myocardial contractility in the regulation of cardiac performance in human hyperthyroidism. *The Journal of Clinical Endocrinology & Metabolism*, 87(3):968–974, 2002.
- [11] Harisios Boudoulas, Parashos Geleris, Richard P Lewis, and Stanley E Rittgers. Linear relationship between electrical systole, mechanical systole, and heart rate. *Chest*, 80(5):613–617, 1981.
- [12] Felix Breitenecker, Andreas Körner, Martin Bicher, Nikolas Popper, Stefanie Winkler, and Günter Schneckenreither. Lecture notes in Modeling and Simulation. January. *Institute for Analysis and Scientific Computing, Technische Universität Wien*, 2016.
- [13] Michael Brennan, Marimuthu Palaniswami, and Peter Kamen. Do existing measures of poicare plot geometry reflect nonlinear features of heart rate variability? *IEEE transactions on biomedical engineering*, 48(11):1342–1347, 2001.
- [14] Michael Brennan, Marimuthu Palaniswami, and Peter Kamen. Poincare plot interpretation using a physiological model of hrv based on a network of oscillators. *American Journal of Physiology-Heart and Circulatory Physiology*, 283(5):H1873–H1886, 2002.
- [15] Michael Brennan, Marimuthu Palaniswami, and Peter W Kamen. A new cardiac nervous system model for heart rate variability analysis. In *Engineering in Medicine and Biology Society, 1998. Proceedings of the 20th Annual International Conference of the IEEE*, pages 349–352. IEEE, 1998.

- [16] Herbert Büning and Götz Trenkler. *Nichtparametrische statistische methoden*. 1998.
- [17] Stephen Butterworth. On the theory of filter amplifiers. *Wireless Engineer*, 7(6):536–541, 1930.
- [18] Taolue Chen, Marco Diciolla, Marta Kwiatkowska, and Alexandru Mereacre. A simulink hybrid heart model for quantitative verification of cardiac pacemakers. In *Proceedings of the 16th international conference on Hybrid systems: computation and control*, pages 131–136. ACM, 2013.
- [19] Wikimedia Commons. File:2033 depolarization in sinus rhythm.jpg, 2013. Available at https://commons.wikimedia.org/wiki/File:2033_Depolarization_in_Sinus_Rhythm.jpg, accessed 2018-10-07.
- [20] Richard W DeBoer, John M Karemaker, and Jan Strackee. Hemodynamic fluctuations and baroreflex sensitivity in humans: a beat-to-beat model. *American Journal of Physiology-Heart and Circulatory Physiology*, 253(3):H680–H689, 1987.
- [21] John R Dormand and Peter J Prince. A family of embedded runge-kutta formulae. *Journal of computational and applied mathematics*, 6(1):19–26, 1980.
- [22] Anthony Dupre, Sarah Vincent, and Paul A Iaizzo. Basic ecg theory, recordings, and interpretation. In *Handbook of cardiac anatomy, physiology, and devices*, pages 191–201. 2005.
- [23] Dwain L Eckberg. Point: counterpoint: respiratory sinus arrhythmia is due to a central mechanism vs. respiratory sinus arrhythmia is due to the baroreflex mechanism. *Journal of applied physiology*, 106(5):1740–1742, 2009.
- [24] Task Force of the European Society of Cardiology the North American Society of Pacing Electrophysiology. Heart rate variability: standards of measurement, physiological interpretation, and clinical use. *Circulation*, 93(5):1043–1065, 1996.
- [25] Arthur Guyton and John Hall. *Textbook of medical physiology*, 11th, 2006.
- [26] Klemens Hocke. Phase estimation with the lomb-scargle periodogram method. In *Annales Geophysicae - European Geophysical Society*, volume 16, pages 356–358. Springer Verlag KG, 1998.

- [27] Peter Walter Kamen, Henry Krum, and Andrew Maxwell Tonkin. Poincare plot of heart rate variability allows quantitative display of parasympathetic nervous activity in humans. *Clinical science*, 91(2):201–208, 1996.
- [28] Hubert W Lilliefors. On the kolmogorov-smirnov test for normality with mean and variance unknown. *Journal of the American statistical Association*, 62(318):399–402, 1967.
- [29] Thomas E Lohmeier and Radu Iliescu. The baroreflex as a long-term controller of arterial pressure. *Physiology*, 30(2):148–158, 2015.
- [30] Marek Malik. Heart rate variability. *Annals of Noninvasive Electrocardiology*, 1(2):151–181, 1996.
- [31] Martial M Massin, Krystel Maeyns, Nadia Withofs, Françoise Ravet, and Paul Gérard. Circadian rhythm of heart rate and heart rate variability. *Archives of disease in childhood*, 83(2):179–182, 2000.
- [32] Javier Mateo and Pablo Laguna. Improved heart rate variability signal analysis from the beat occurrence times according to the ipfm model. *IEEE Transactions on Biomedical Engineering*, 47(8):985–996, 2000.
- [33] Laurie Kelly McCorry. Physiology of the autonomic nervous system. *American journal of pharmaceutical education*, 71(4):78, 2007.
- [34] Rollin McCraty and Fred Shaffer. Heart rate variability: new perspectives on physiological mechanisms, assessment of self-regulatory capacity, and health risk. *Global Advances in Health and Medicine*, 4(1):46–61, 2015.
- [35] Des McLernon, Nader Jafarnia Dabanloo, Ahmad Ayatollahi, Vahid Johari Majd, and Henggui Zhang. A new nonlinear model for generating rr tachograms. In *Computers in Cardiology, 2004*, pages 481–484. IEEE, 2004.
- [36] Olivier Meste, Balkine Khaddoumi, Gregory Blain, and Stephane Bermon. Time-varying analysis methods and models for the respiratory and cardiac system coupling in graded exercise. *IEEE transactions on biomedical engineering*, 52(11):1921–1930, 2005.
- [37] Nobuyuki Miyai, Mikio Arita, Kazuhisa Miyashita, Ikuharu Morioka, Tatsuo Shiraishi, and Ichiro Nishio. Blood pressure response to heart rate during exercise test and risk of future hypertension. *Hypertension*, 39(3):761–766, 2002.

- [38] Mette S Olufsen and Ali Nadim. -on deriving lumped models for blood flow and pressure in the systemic arteries. In *Computational Fluid and Solid Mechanics 2003*, pages 1786–1789. 2003.
- [39] Mette S Olufsen, Hien T Tran, Johnny T Ottesen, Lewis A Lipsitz, and Vera Novak. Modeling baroreflex regulation of heart rate during orthostatic stress. *American Journal of Physiology-Regulatory, Integrative and Comparative Physiology*, 291(5):R1355–R1368, 2006.
- [40] OECD/European Observatory on Health Systems and Policies. Austria: Country health profile 2017. In *State of Health in the EU*. OECD Publishing, Paris/European Observatory on Health Systems and Policies, Brussels, 2017.
- [41] Hans-Christian Pape, Armin Kurtz, and Stefan Silbernagl. *Physiologie*. 2018.
- [42] Stephanie Parragh. *Modelle zur Bestimmung des aortalen Blutflusses basierend auf Optimalitätsbedingungen*. Master’s thesis, TU Wien, Institut für Analysis und Scientific Computing, 2013.
- [43] Henrik Seidel and Hanspeter Herzel. Modelling heart rate variability due to respiration and baroreflex. In *Modelling the Dynamics of Biological Systems*, pages 205–229. 1995.
- [44] Lawrence F Shampine and Mark W Reichelt. The matlab ode suite. *SIAM journal on scientific computing*, 18(1):1–22, 1997.
- [45] Robert E Shannon. Systems simulation; the art and science. Technical report, 1975.
- [46] Stefan Silbernagl and Agamemnon Despopoulos. *Taschenatlas Physiologie*. 2007.
- [47] Garrett B Stanley, Kameshwar Poola, and Ronald A Siegel. Threshold modeling of autonomic control of heart rate variability. *IEEE Transactions on Biomedical Engineering*, 47(9):1147–1153, 2000.
- [48] Malvin C Teich, Steven B Lowen, Bradley M Jost, Karin Vibe-Rheymer, and Conor Heneghan. Heart rate variability: measures and models. *arXiv preprint physics/0008016*, 2000.
- [49] Julian F Thayer and Richard D Lane. A model of neurovisceral integration in emotion regulation and dysregulation. *Journal of affective disorders*, 61(3):201–216, 2000.

- [50] Nick Townsend, Lauren Wilson, Prachi Bhatnagar, Kremlin Wickramasinghe, Mike Rayner, and Melanie Nichols. Cardiovascular disease in europe: epidemiological update 2016. *European heart journal*, 37(42):3232–3245, 2016.
- [51] Ken Umetani, Donald H Singer, Rollin McCraty, and Mike Atkinson. Twenty-four hour time domain heart rate variability and heart rate: relations to age and gender over nine decades. *Journal of the American College of Cardiology*, 31(3):593–601, 1998.
- [52] Mauro Ursino. Interaction between carotid baroregulation and the pulsating heart: a mathematical model. *American Journal of Physiology-Heart and Circulatory Physiology*, 275(5):H1733–H1747, 1998.
- [53] Hedde Van de Vooren, Maaïke GJ Gademan, Cees A Swenne, Ben J TenVoorde, Martin J Schalijs, and Ernst E Van der Wall. Baroreflex sensitivity, blood pressure buffering, and resonance: what are the links? computer simulation of healthy subjects and heart failure patients. *Journal of Applied Physiology*, 102(4):1348–1356, 2007.
- [54] Charles Antzelevitch Victor S Reiner. Phase resetting and annihilation in a mathematical model of sinus node. *American Journal of Physiology-Heart and Circulatory Physiology*, 249(6):H1143–H1153, 1985.
- [55] Nico Westerhof, Jan-Willem Lankhaar, and Berend E Westerhof. The arterial windkessel. *Medical & biological engineering & computing*, 47(2):131–141, 2009.
- [56] Fumihiko Yasuma and Jun-ichiro Hayano. Respiratory sinus arrhythmia: why does the heartbeat synchronize with respiratory rhythm? *Chest Journal*, 125(2):683–690, 2004.